การกดแบบแข็งเกร็งไร้แรงเสียดทานบนกึ่งปริภูมิโดยพิจารณาหน่วยแรงที่ผิว

นางสาว ยุติวดี ภิญโญโชติวงศ์

RIGID FRICTIONLESS INDENTATION ON HALF-SPACE
WITH SURFACE STRESSES

Miss Yutiwadee Pinyochotiwong

A Thesis Submitted in Partial Fulfillment of the Requirements

for the Degree of Master of Engineering Program in Civil Engineering

Department of Civil Engineering

Faculty of Engineering

Chulalongkorn University

Academic Year 2010

Thesis Title	RIGID FRICTIONLESS INDENTATION ON HALF-SPACE WITH SURFACE STRESSES
By	Miss Yutiwadee Pinyochotiwong
Field of Study	Civil Engineering
Thesis Advisor	Assistant Professor Jaroon Rungamornrat, Ph.D.
Thesis Co-advisor	Professor Teerapong Senjuntichai, Ph.D.

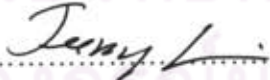
Accepted by the Faculty of Engineering, Chulalongkorn University in Partial Fulfillment of the Requirements for the Master's Degree

.... Dean of the Faculty of Engineering

(Associate Professor Boonsom Lerdhirunwong, Dr.Ing.)

THESIS COMMITTEE

.... Chairman

(Assistant Professor Watanachai Smittakorn, Ph.D.)

.... Thesis Advisor

(Assistant Professor Jaroon Rungamornrat, Ph.D.)
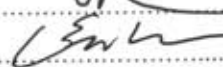
.... Thesis Co-advisor

(Professor Teerapong Senjuntichai, Ph.D.)

.... External Examiner

(Associate Professor Pruettha Nanakorn, D.Eng)

ยุติวดี   ภิญโญโชติวงศ์ : การกดแบบแข็งเกร็งไร้แรงเสียดทานบนกึ่งปริภูมิโดยพิจารณาหน่วยแรงที่ผิว. (RIGID FRICTIONLESS INDENTATION ON HALF-SPACE WITH SURFACE STRESSES) อ. ที่ปรึกษาวิทยานิพนธ์หลัก : ผู้ช่วยศาสตราจารย์ ดร.จรูญ รุ่งอมรรัตน์, อ. ที่ปรึกษาวิทยานิพนธ์ร่วม : ศาสตราจารย์ ดร.ธีรพงศ์ เสนจันทร์ฒิไชย, 60 หน้า.

วิทยานิพนธ์ฉบับนี้นำเสนอการพัฒนาสมการกำกับและวิธีการหาผลเฉลยของปัญหาการกดแบบแข็งเกร็ง ไร้แรงเสียดทานที่มีความสมมาตรรอบแกนบนกึ่งปริภูมิโดยพิจารณาหน่วยแรงที่ผิว ลักษณะเด่นของสมการ กำกับที่พัฒนาขึ้นคือการใช้สมการของเกอร์ดินและเมอร์ดอครูปแบบสมบูรณ์ในการจำลองพฤติกรรมของหน่วย แรงที่ผิว โดยอาศัยหลักการตัวแทนความเครียดศักย์ของเลิฟร่วมกับการแปลงแฮนเคล   ปัญหาค่าขอบเขต ดังกล่าวสามารถลดรูปเป็นสมการคู่ปริพันธ์ที่สอดคล้องกับค่าขอบเขตผสมที่พื้นผิวกึ่งปริภูมิ หลังจากที่แปลง สมการคู่ปริพันธ์ดังกล่าวเป็นสมการปริพันธ์เฟรดโฮล์มชนิดที่สองเพียงสมการเดียวแล้ว สามารถหาผลเฉลยเชิง ตัวเลขของสมการปริพันธ์เฟรดโฮล์มโดยใช้วิธีประมาณรูปแบบผลเฉลยร่วมกับระเบียบวิธีคอลโลเคชัน ผลเฉลย ของระบบสมการเชิงเส้นที่ได้จากขั้นตอนการประมาณสามารถคำนวณได้โดยใช้ระเบียบวิธีเชิงตัวเลขที่เหมาะสม และผลเฉลยดังกล่าวนี้สามารถนำไปใช้ในการคำนวณปริมาณสนามยืดหยุ่นเพื่อเปรียบเทียบผลการกดที่เกิด จากรูปร่างและรัศมีการกดที่แตกต่างกันที่ระดับความลึกต่างๆ เพื่อศึกษาพฤติกรรมที่ขึ้นอยู่กับขนาดของวัสดุ และอิทธิพลของหน่วยแรงที่ผิวที่มีต่อหน่วยแรงและการเคลื่อนที่ของกึ่งปริภูมิโดยเฉพาะตรงบริเวณที่ใกล้กับผิว อิสระของกึ่งปริภูมิและใกล้กับหัวกด บทบาทของแรงดึงผิวคงค้างที่มีผลอย่างมากต่อคุณสมบัติวัสดุแสดงให้เห็น ถึงความสำคัญของการพิจารณาอิทธิพลของหน่วยแรงที่ผิวที่มีต่อคุณสมบัติของวัสดุสำหรับของแข็งนิ่มยืดหยุ่น และวัสดุระดับนาโน

ภาควิชา ....วิศวกรรมโยธา............. ลายมือชื่อนิสิต ....ยุติวดี..ภิญโญโชติวงศ์........

สาขาวิชา ....วิศวกรรมโยธา............. ลายมือชื่ออ.ที่ปรึกษาวิทยานิพนธ์หลัก ....

ปีการศึกษา ....2553................ ลายมือชื่ออ.ที่ปรึกษาวิทยานิพนธ์ร่วม ....

5270722521 : MAJOR CIVIL ENGINEERING

KEYWORDS : NANOINDENTATION / MIXED BOUNDARY VALUE PROBLEMS / SURFACE STRESSES / GURTIN-MURDOCH MODEL / HALF-SPACE

YUTIWADEE PINYOCHOTIWONG : RIGID FRICTIONLESS INDENTATION ON HALF-SPACE WITH SURFACE STRESSES. ADVISOR : ASSISTANT PROFESSOR JAROON RUNGAMORNRAT, Ph.D., CO-ADVISOR : PROFESSOR TEERAPONG SENJUNTICHAI, Ph.D., 60 pp.

The formulation and solutions of a boundary value problem of an axisymmetric, rigid, frictionless indentation acting on an elastic half-space is presented. The novel feature of the formulation is associated with the treatment of surface energy effects by employing a *complete* Gurtin-Murdoch continuum model for surface elasticity. With use of standard Love's representation and Hankel integral transform, such boundary value problem can be reduced into a set of dual integral equations associated with the mixed boundary conditions on the surface of the half-space. Once these dual integral equations are transformed into a Fredholm integral equation of the second kind, selected numerical procedures based upon solution discretization and a collocation technique are proposed to construct its solution numerically. After solving a system of linear algebraic equation arising from the discretization, numerical results for elastic fields are obtained and compared for indentations of different profiles and contact radii at various depths to show the size-dependency and influence of surface free energy on bulk stresses and displacements especially in the vicinity of the free surface. The significant contribution of the residual surface tension suggests that the surface energy effects have to be accounted for characterization of soft elastic solids and nanoscale material properties.

Department: ......Civil Engineering....... Student 's Signature: ยุติวดี..ลิญโฌโซติวงศ์

Field of Study: ..Civil Engineering....... Advisor 's Signature: ....

Academic Year: ....2010.............. Co-advisor 's Signature:

ACKNOWLEDGEMENTS

CONTENTS

LIST OF TABLES

LIST OF FIGURES

LIST OF ABBREVIATIONS

a	radius of contact area
d	indentation depth
J_n	n-th order Bessel function of the first kind
n_i	unit normal vector in the i-direction
P	indentation force
r	radial coordinate
t_i^0	prescribed traction on the surface in the i-direction
u_i	displacement component of the bulk in the i-direction
z	vertical coordinate
α	characteristic parameter of the paraboloidal punch
$\delta(r)$	profile of the punch
δ_{ij}	Kronecker delta
ε_{ij}	strain components
κ^s	surface elastic modulus
μ , λ	Lamé's constants of the bulk material
μ^s , λ^s	Lamé's constants of the surface material
ϕ	solution of a Fredholm integral equation
σ_{ij}	stress components
τ^s	residual surface tension under unconstrained conditions
ξ	Hankel transform parameter
Φ	Love's strain potential
Λ_0	material characteristic length

CHAPTER I

INTRODUCTION

1.1 General

Nanotechnology has remarkably become one of the most interesting fields in biology, chemistry, physics and engineering in recent years. Nanoshell, an example of a newly nanoscale innovation in fields of medicine and healthcare, can float through human body and destroy the tumor just after being activated by a laser beam without harming surrounding healthy cells. Patients will benefit greatly from this kind of technology as it makes the diagnostics faster yet cheaper. In energy sector, future household lightings will apply nanocrystals to transform electricity into light instead of wasting away into heat. For public utilities, nanotechnology will provide efficient water purification techniques, allowing inhabitants in third-world countries to access clean water (Booker and Boysen, 2005). It is undeniable that nanotechnology will leverage our standard of living and become the next industrial revolution (Ratner and Ratner, 2002).

In order to meet those human needs circumspectly, the advanced researches on material properties of nanostructured materials and nanosized structural elements such as nanotubes, nanowires, nanocomposites and nanofilms have been rapidly reported in every important aspect. For instance, upon the discovery of carbon nanotube (CNT) in 1991 by Iijima (Iijima, 1991; Iijima and Ichihashi, 1993), CNT has been experimented and presently known as the ideal material that possess excellent mechanical properties, i.e. Young's modulus, tensile strength and failure strains of detect-free single-walled CNT are up to 1 TPa, 100 GPa and 15-30%, respectively (Peng et al., 2008). Useful information about physical and mechanical properties of materials at nanoscale level is essential for designing realistic microelectromechanical systems (MEMS) and nanoelectromechanical systems (NEMS) devices. Nanocrystalline silicon carbide films, as an obvious example, have large hardness values and could have great applications in producing hard protective coatings for

cutting tools, and computer hard disks (Liao et al., 2005). Moreover, silicon carbide possess higher Young's modulus to mass density ratio than other semiconducting materials (e.g. Si and GaAs), it becomes an ideal semiconductor for device applications requiring high frequency mechanical response (Yang et al., 2001).

Nanomechanical properties can be investigated by two basic approaches, namely, experimental methods and theoretical simulations. Some of previous studies using direct experimental methods include, for example, the work of Wong et al. (1997) in the determination of mechanical properties of isolated silicon carbide (SiC) nanorods (NRs) and multi-wall carbon nanotubes (MWNTs) by using atomic force microscopy. They suggested that Sic NRs with smaller Young's modulus should be used as a reinforcing material in some composite structures instead of using carbon nanotubes whereas applications of MWNTs with ability to store or absorb considerable energy should be in armor. Mao et al. (2003) tested a single nanobelt of ZnO and SnO_2 under an atomic force microscope and found that the hardness of the ZnO nanobelt is less than that of SnO_2. Poncharal et al. (1999) also measured the bending modulus of carbon nanotubes statically and dynamically in a transmission electron microscope. Such experiments revealed that the elastic bending modulus as a function of diameter is found to decrease sharply with increasing diameter, providing direct evidence of the size dependence of elastic properties at the atomic scale.

Another approach is based upon the mathematical modeling. Two predominant models commonly employed to simulate various phenomena in solids are molecular and continuum models. Though molecular simulations offer advantages in precise response prediction because of their effectiveness in detailing of bonds or atoms, but they need tremendous computation effort associated with the need to model billions of atoms at a nanoscale and hence they are limited in practical application. Therefore, the continuum-based approach is considered attractive since it dramatically reduces the computational cost with lesser complexity. To be in agreement with the response obtained from an atomistic model, the effects that exist at the nanoscale have to be accounted properly in a classical continuum model. Recent atomistic computations indicate that atoms near a free surface behave differently from

those of the bulk. In this sense, all structural elements are not strictly homogeneous, but when the size of elements is in micrometers or larger, the effect of surface free energy is commonly neglected due to the fact that it does not have significant influence on overall properties. For nanoscale elements, unlike macroscale elements, the surface to volume ratio is much higher and the effect of surface free energy subsequently becomes significant. Thus, to explain the size-dependent behavior at the nanoscale upon the continuum concept, several researchers have attempted to incorporate the concept of surface free energy into classical continuum models. For example, He et al. (2004) proposed a continuum model based on surface elasticity to analyze the size-dependent mechanical response of ultra-thin elastic films of nanoscale thickness. Recently, Wang et al. (2010) investigated the size-dependent deformations of two-dimensional nanosized structures with surface effects by employing the finite element method. They implemented Gurtin and Murdoch surface elasticity model with ANSYS through its user programmable features and reported that the effective elastic moduli of an elastic solid containing nanoscale circular voids is size-dependent. Noticeably, all of these fields of researches have demonstrated how the surface elasticity model applies to show mechanical responses of materials at the nanoscale level.

Due to the rapid growth on development of small-scale devices such as sensors and actuators, research involving the characterization of material properties at nanoscale has recently gained significant attention from various investigators. Nanoindentation has now become a widely adopted technique to be used in the measurement of mechanical properties, such as hardness and elastic modulus, at the nanoscale in the past decade. Unfortunately, the effect of surface elasticity during the indentation has been usually considered by experimental measurements and molecular dynamics/atomistic simulations which are generally very time-consuming and expensive. To minimize such limitations, modified continuum models accounted for the surface effects could be developed for nanoindentation problems, additionally, in order to clearly understand the mechanical properties of soft elastic solids.

In following sections, previous studies related to the surface elasticity model and indentation problems are presented in order to demonstrate the current advances of this field and identify the gap of knowledge to be focused on in the present investigation.

1.2 Background and Review

In this section, an extensive literature survey including the existing work relevant to the current study and the sequence of historical background in this specific area is provided. In order to be systematic, results from such overview are separated into two parts regarding to their main focus. Firstly, the development of surface elasticity model is reviewed to observe how important of surface energy effects in the material characterization of nanoscale elements and soft elastic solids. Then, previous studies related to indentation problems, both with and without the surface stress effects, are presented and discussed.

1.2.1   Review of Surface Elasticity Model

Gibbs (1906), who originally formulated the most useful and powerful concepts in studying surface phenomena, defined the quantity γ that represents the excess free energy per unit area owing to the existence of a surface. Gibbs was the first who pointed out that, for solid-solid interfaces, there is another type of fundamental parameter called the surface stress that critically affects the behavior of surfaces, i.e. to elastically stretch a pre-existing surface. Simply saying that, to deform such a solid, excessive work is needed to stretch the surface in addition to straining the bulk. The larger partition of work done to surface, the more important the effect of surface stress (He and Lim, 2006). Comprehensive literature review on the surface energy effect and the Gibbsian formulation of the thermodynamics of surfaces can be found in general researches of surface and interface stresses (Cammarata, 1994; Cammarata, 1997; Shuttleworth, 1950; Fischer et al., 2008). Especially, Cammarata (1994) gave an excellent explanation of the concept of the surface stress and also showed that the difference between the surface stress and the surface free energy γ is equal to the change in surface free energy per unit change in elastic strain of the

surface. It should be noted that γ is a scalar quantity, while the surface stress is a second order tensor in the tangent plane of the surface and the strain normal to the surface is excluded.

A surface can be identified as a layer that an excess energy is attached and certain energy is usually termed as the surface energy γ (Fischer et al., 2008). Due to the different number of nearest neighbors between surface atoms and bulk atoms, it results a corresponding redistribution of electronic charge and modifies layer spacing to be lesser at the surface which deviates from the bulk value (Sander, 2003). As a result, the energy at a free surface will, in general, be different from that of the atoms in the bulk (Dingreville et al., 2005). The ratio of surface free energy γ (J/m^2) and Young's modulus E (J/m^3), γ/E, is an inevitable parameter of materials (Yakobson, 2003). For usual metallic materials, the ratio is normally less than one Angstrom. For some soft solids, such as polymer gels and biological materials, however, the surface energy (or surface stress) is a little less than that of a metal, but the elastic modulus can be nearly 7-8 orders smaller than that of conventional solids. Therefore, the corresponding intrinsic length scale of soft solids is much larger, implying that the surface energy can play an important role on the properties of the materials, and thus the properties become size-dependent (He and Lim, 2006). As a consequence, the effects of surface stress should be extremely incorporated into classical continuum models in order to study the behavior of soft materials or to obtain the correct response for nanoscale problems.

Many authors have developed continuum models that include surface energy effects, and one of them is Gurtin-Murdoch model. Gurtin and Murdoch (1975, 1978), and Gurtin et al. (1998) proposed a mathematical framework to study the mechanical behavior of material surfaces through a continuum model with the surface stress. An elastic surface is assumed to be very thin and modeled as a mathematical layer of zero thickness bonded to the bulk without slipping. Also, the elastic moduli of the surface can be different from the bulk. For an isotropic elastic surface, a linearized surface stress-strain constitutive relation is given by

$$\sigma_{\beta\alpha}^{s} = \tau^{s}\delta_{\beta\alpha} + 2\left(\mu^{s} - \tau^{s}\right)\varepsilon_{\beta\alpha}^{s} + \left(\lambda^{s} + \tau^{s}\right)\varepsilon_{\gamma\gamma}^{s}\delta_{\beta\alpha} + \tau^{s}u_{\beta,\alpha}^{s} \tag{1.1}$$

where the subscript 's' denotes the quantities corresponding to the surface, μ^{s} and λ^{s} are surface Lamé constants and τ^{s} is the residual surface tension under unstrained conditions, which is a constant.

In order to verify Gurtin-Murdoch model, Miller and Shenoy (2000) employed such a model to describe the size dependence of the stiffness of plates, bars and beams under either uniaxial tension or bending. Their results were compared with direct atomistic simulations of nanoscale structures using the embedded atom method for face-centered cubic aluminum and the Stillinger–Weber model for silicon. By neglecting the error induced from the effects of corners present in the modeling of beams, excellent agreement between the simulations and the model is observed. Shenoy (2002) completed a framework derived earlier by Miller and Shenoy (2000) by adding the torsional rigidities of nanosized structural elements and applied to the case of nanoscale bars in torsion. The theoretical results were compared with direct atomistic simulations for the torsion of square bars of various metals and found in good agreement. It is noted that the difference in theoretical values and simulation results mainly came from the assumption that the surface energy depends only on the surface strain; however, it should also depend on the surface curvature strain. Dingreville et al. (2005) derived analytical expressions for an elastic modulus tensor of nanosized structural elements accounted for surface energy effects and showed that the overall elastic properties of nanosized particles, wires and films are size-dependent. The effective Young's modulus of thin films of various thicknesses computed by using molecular static (MS) simulations and their proposed formulation found in excellent agreement. They also pointed out that results obtained from MS simulations were much more computationally intensive than the proposed formulation. This should confirm the benefit of employing such alternative continuum-based model to save the computational resources. Undoubtedly, Gurtin-Murdoch continuum model has been applied and widely used in nanoscale problems by several investigators, for example, to analyze the size dependent mechanical response of ultra-thin elastic films (He et al., 2004; Huang, 2008) and thin plates (Lu

et al., 2006). Recently, such a model has been employed to study the problems of nanoscale inhomogeneities. For instance, Sharma and Wheeler (2007) and Sharma et al. (2003) reformulated the size dependent elastic field of spherical and ellipsoidal nano-inclusions by applying this model. Duan et al. (2005) presented the interior and exterior Eshelby tensors for a spherical inhomogeneity subjected to arbitrary uniform eigenstrain under the surface/interface effects. Tian and Rajapakse (2007a, 2007b) derived the solution for a nanoscale circular and elliptical inhomogeneity in an infinite matrix under remote loading based on the Gurtin-Murdoch model. Moreover, Zhao and Rajapakse (2009) presented the analytical solution of the plane and axisymmetric problems for an elastic layer of finite thickness subjected to surface loading by using Fourier and Hankel Transform techniques. Numerical results indicated that the surface effects show significant influence on the vertical surface displacement of a layer and such influence on the stress field in the case of horizontal point load is more significant than that in the case of vertical point load. Intarit et al. (2010) recently confirmed the significance of the surface stress on very near the surface of both shear and opening dislocations, and also on buried vertical and horizontal loads in an elastic half-plane. They also found that the stress field has an asymptotic solution with increasing the characteristic length parameter.

It is obviously seen from (1.1) that, to employ Gurtin-Murdoch continuum model, surface elastic properties (i.e. surface energy, surface stress, and surface elastic stiffness) must be known a priori. In addition, these particular quantities are also strongly influenced on the overall mechanical behavior in nanostructures. Thus, many approaches have been proposed, based either on experimental measurements or atomistic simulations, to determine such properties. Among various experimental techniques, Jing et al. (2006) measured the elastic properties of the nanowires by using contact atomic force microscopy (C-AFM) and found that the Young's modulus of the silver nanowire with consideration of the surface effect, surface modulus and surface stress are 56 GPa, 8.7 N/m and 5.8 N/m, respectively. Another method, rather computationally intensive, is atomistic simulations. Shenoy (2005) developed a fully nonlinear formulation of the surface elasticity and established a procedure for calculating surface elastic constants from atomistic simulations by adopting the

embedded atom method. To reduce disadvantages of both experimental and atomistic approaches, Dingreville and Qu (2007) presented a semi-analytical method to compute a full set of data on surface elastic properties of crystalline materials. By applying this developed method, the surface elastic properties were formulated analytically and explicitly in terms of inter-atomic potentials, and a standard molecular simulation was used to obtain the relaxed positions of the atoms near the free surface in order to evaluate such analytical expressions.

1.2.2 Review of Indentation Problems

It is understood that indentation techniques have been widely used for measuring mechanical properties on nanoscale such as hardness and elastic modulus. For example, the use of nanoindentation to measure the mechanical properties of ceramics (Hainsworth and Page, 1994), metals (Armstrong et al., 1995; Beegan et al., 2007) and polymers (Yang and Li, 1995; Yang and Li, 1997). By using depth-sensing indentation tests with either spherical or conical indenters, Young's modulus can be calculated from the slope of the linear portion of the unloading curves in the load versus penetration depth while hardness can be calculated from data along the loading curves (Doerner and Nix, 1986; Oliver and Pharr, 1992).

Several authors have obtained the elastic solution of the indentation problems by using various mathematical methods. The classical problem of axisymmetric rigid punch indenting on an elastic half-space seems to be first considered by Boussinesq (Boussinesq, 1885). According to the form of a solution, his numerical results were derived only for a flat-ended cylindrical and a conical punch. Harding and Sneddon (1945) and Sneddon (1965) solved Boussinesq's problem under a punch of arbitrary profile by applying Hankel integral transform techniques. Clements (1971) later determined the stress fields produced from the rigid indentation on an anisotropic half-space by employing the theory of anisotropic elasticity developed by Eshelby et al. (1953) and Stroh (1958). Since the smart materials have recently gained significant interest from several researchers in the field of mechanics, the classical theory of elasticity becomes an important tool in studying their behavior from indentation techniques. Chen (2000) generalized the potential theory to analyze the piezoelastic

contact problem of a punch pressed against a piezoelectric half-space. Giannakopoulos and Parmaklis (2007) examined the quasistatic contact problem of a circular rigid punch on piezomagnetic materials and confirmed their theoretical results by conducting an experiment on Terfenol-D. Moreover, an elastic behavior of a nonhomogeneous transversely isotropic half-space was studied by Chaudhuri and Ray (2003) under the action of a smooth rigid axisymmetric indenter.

The indentation problems associated with an elastic layer perfectly bonded to an elastic half-space have also been investigated. Lebedev and Ufliand (1958) considered a problem of a flat-ended rigid cylindrical indenter on an elastic layer resting on a rigid foundation by using Papkovich-Neuber's representation for the displacement vector. After reducing mixed boundary conditions to a pair of integral equations, Fredholm integral equation was obtained and solved numerically. By taking the Hankel transform technique, Dhaliwal and Rau (1970) reduced the axisymmetric Boussinesq problem of an elastic layer lying over an elastic half-space under a rigid punch of arbitrary profile to a Fredholm integral equation but no numerical result was presented in their study. Subsequently, Rau and Dhaliwal (1972) developed a numerical technique to solve the integral equation developed by Dhaliwal and Rau (1970) and obtained the complete elastic field. Yu et al. (1990) presented numerical results obtained from solving Fredholm integral equation of the second kind to demonstrate the effect of a substrate on the elastic properties of films and provided useful guidelines for the proper choice of an approximate layer thickness and substrate elastic properties to determine the elastic constants of the layer. Motivated by a recently developed multi-dimensional nanocontact system (Lucas et al., 2003), Gao et al. (2008) gave an analytical formulation by applying Green's function in Fourier space to predict the effective elastic modulus of film-on-substrate systems under normal and tangential contact. In addition, Yang (1998) studied the problem of impressing a rigid flat-ended cylindrical indenter onto an incompressible elastic film by following a standard procedure such that the Hankel transformation was applied to the mixed boundary conditions and the Fredholm integral equation of the second kind was subsequently solved numerically.

The surface stress effect on mechanical responses of nanoindentation has been recently studied by applying the Gurtin-Murdoch continuum model. Zhao (2009) derived an analytical solution of a classical indentation problem in the presence of the surface energy effect. By applying Gurtin-Murdoch continuum model, he obtained a solution for elastic fields within the half-space caused by flat-ended cylindrical, conical and spherical rigid indenters. Although Gurtin-Murdoch continuum model used in his formulation is not complete (e.g. no out-of-plane term), obtained numerical solutions still showed a size-dependent behavior due to the presence of surface energy effect, i.e. when the contact area becomes smaller, the material behaves stiffer. In addition, it is remarked that atomistic simulations (Sinnott et al., 1997; Liu et al., 2007; Chen et al., 2008; Lu et al., 2009) can also be used to investigate the mechanism of an indentation process under different indenter shapes (i.e. spherical indenter and pyramidal indenter), sizes and indentation loads on interested materials. In this approach, applied molecular dynamics theory is employed to finally obtain the mechanical properties such as hardness and load-displacement curves.

As mentioned in the introduction and extensive review of existing works in this area, the influence of surface energy effects by using a complete set of Gurtin-Murdoch continuum model in order to capture the size-dependent behavior of nano-indention problems has not been investigated. This therefore requires profound exploration to further enhance the correct elastic fields accounted for surface effects.

1.3 Research Objective

The key objective of this research is to investigate mechanical responses of a rigid punch acting on a half-space with consideration of surface energy effects.

1.4 Research Scopes

The proposed investigation is to be carried out within following context:

1) A rigid punch is frictionless and possesses an axisymmetric profile.
2) A half-space (bulk) material is homogeneous, isotropic and linearly elastic.

3) The influence of the surface energy effects is treated by using complete Gurtin-Murdoch surface elasticity model.

1.5 Research Methodology

1) A corresponding axisymmetric mixed boundary value problem is formulated and reduced to a set of dual integral equations by using Hankel integral transform.

2) Dual integral equations are further reduced to a Fredholm integral equation of the second kind by using a procedure based on Sonine's integrals.

3) Selected numerical techniques are adopted to solve resulting Fredholm integral equation of the second kind.

4) Once the solution of such Fredholm integral equation is obtained, Hankel transform inversions are then employed to determine elastic fields and other interesting quantities (i.e. contact pressure and indentation force).

1.6 Research Significance

The current investigation proposes an application of continuum-based concepts in the analysis of indentation problems for nanoscale structures and soft elastic solids by incorporating surface energy effects into a classical continuum model. With use of complete Gurtin-Murdoch surface elasticity model, proposed formulation is applicable to perform the existence of an inevitable parameter of materials via size-dependent behavior and also to strongly demonstrate the influence of out-of-plane contribution of residual surface tension on material stiffness. When compared with molecular dynamics simulations, this modified continuum model is an alternative approach in terms of dramatically reduction in computational resources with an acceptable level of accuracy. Such attractive approach offers an alternative for studying the mechanical properties and mechanical deformation for punches of arbitrary axisymmetric profiles. In addition, knowledge and findings from the present study should provide a crucial basis and guidelines for further investigations in the area of nanomechanics.

CHAPTER II

THEORETICAL CONSIDERATIONS

In this chapter, the formulation of boundary value problem associated with an axisymmetric, frictionless, rigid punch acting on a half-space (with consideration of surface energy effects) is first presented. The Hankel transform is then applied to reduce the corresponding mixed boundary conditions to a set of dual integral equations. These dual integral equations are further reduced to a Fredholm integral equation of the second kind that is well-suited for constructing numerical solutions.

2.1 Problem Statement

(a)   (b)
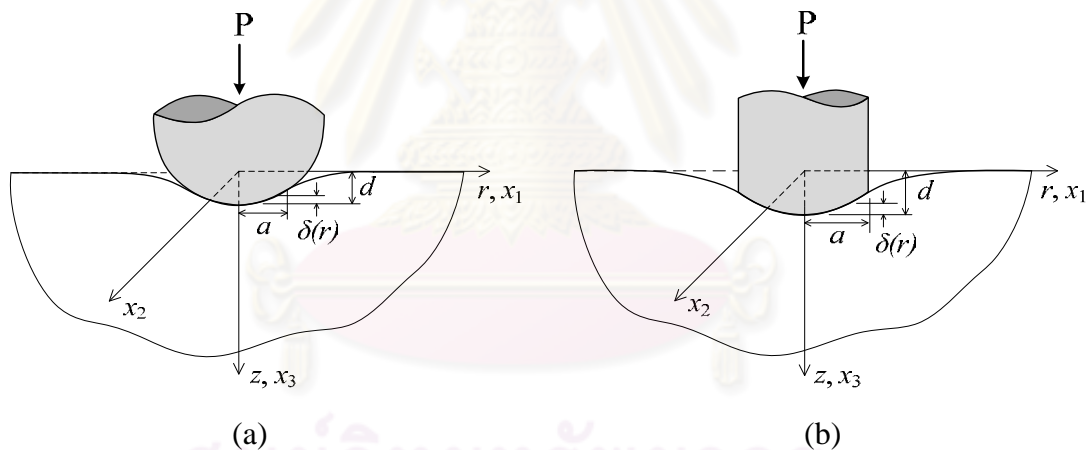
Figure 2.1 Indentation of half-space by axisymmetric rigid frictionless punch:

(a) smooth contact and (b) non-smooth contact

Consider a homogeneous, isotropic, elastic half-space indented by an axisymmetric frictionless rigid punch as shown schematically in Figure 2.1. The profile of the punch, denoted by a function $\delta = \delta(r)$, is defined for convenience and without loss by choosing $\delta = 0$ at $r = 0$. The radius of a contact region and the indentation depth resulting from a resultant force P at the center of the punch are denoted by a and d, respectively. In this study, the profile of the punch is assumed to be smooth (i.e. the unit normal vector to the surface of the punch or, equivalently,

dδ/dr is well-defined) at any point within the contact region except along the boundary *r = a* where the profile is allowed to be non-smooth. A punch with well-defined *dδ/dr* for *r ≤ a* is termed a smooth-contact punch (see Figure 2.1(a)) whereas a punch with well-defined *dδ/dr* only for *r < a* is termed a non-smooth-contact punch (see Figure 2.1(b)). In the present study, the pressure distribution exerted by the punch and the complete elastic fields within the half-space accounted for surface energy effects are to be determined.

2.2 Basic Equations and Formulation of Indentation Problem

Behavior of the half-space (bulk) is governed by a classical theory of elasticity. In the absence of body force, the governing field equations (i.e. equilibrium equations, constitutive relations and strain-displacement relations) can be expressed as

$$\sigma_{ij,j} = 0 \tag{2.1}$$

$$\sigma_{ij} = 2\mu\varepsilon_{ij} + \lambda\delta_{ij}\varepsilon_{kk} \tag{2.2}$$

$$\varepsilon_{ij} = \frac{1}{2}\left(u_{i,j} + u_{j,i}\right) \tag{2.3}$$

where u_i, σ_{ij} and ε_{ij} denote components of the displacement, stress and strain tensors, respectively; δ_{ij} is a Kronecker-delta symbol; and μ and λ are Lamé constants of a bulk material. Note that lower-case indices range from 1 to 3 and repeated indices imply the summation over their range.

A surface of the half-space is regarded as a negligibly thin membrane adhered perfectly to the bulk without slipping and its behavior (which is different from the bulk) is modeled by Gurtin-Murdoch continuum model of surface elasticity. The equilibrium conditions on the surface in terms of the generalized Young-Laplace equation (Povestenko, 1993), surface constitutive relations and strain-displacement relationship, when specialized to this particular case, are given by (Gurtin and Murdoch, 1975; Gurtin and Murdoch, 1978; Gurtin et al., 1998)

$$\sigma^s_{i\alpha,\alpha} + \sigma_{i3} + t^0_i = 0 \tag{2.4}$$

$$\sigma^s_{\beta\alpha} = \tau^s \delta_{\beta\alpha} + 2\left(\mu^s - \tau^s\right)\varepsilon^s_{\beta\alpha} + \left(\lambda^s + \tau^s\right)\varepsilon^s_{\gamma\gamma}\delta_{\beta\alpha} + \tau^s u^s_{\beta,\alpha} \;, \qquad \sigma^s_{3\alpha} = \tau^s u^s_{3,\alpha} \tag{2.5}$$

$$\varepsilon^s_{\alpha\beta} = \frac{1}{2}\left(u^s_{\alpha,\beta} + u^s_{\beta,\alpha}\right) \tag{2.6}$$

where the superscript 's' is used to denote the quantities corresponding to the surface; μ^s and λ^s are surface Lamé constants; τ^s is the residual surface tension under unstrained conditions; and t^0_i denotes the prescribed traction on the surface. It is important to emphasize here that Greek indices range from 1 to 2 and, again, repeated indices imply the summation over their range.

When specialized to an axisymmetric case, the corresponding elastic fields can be obtained by solving, in a cylindrical coordinate system (r, θ, z), the biharmonic equation (Sneddon, 1951; Selvadurai, 2000)

$$\nabla^4 \Phi = 0 \tag{2.7}$$

where $\nabla^2 = \dfrac{\partial^2}{\partial r^2} + \dfrac{1}{r}\dfrac{\partial}{\partial r} + \dfrac{\partial^2}{\partial z^2}$ is the axisymmetric form of Laplace's operator and Φ is Love's strain potential. The displacement and stress fields are given in terms of Φ as follows:

$$\sigma_{rr} = \lambda \nabla^2 \left(\frac{\partial \Phi}{\partial z}\right) - 2(\lambda + \mu)\frac{\partial^3 \Phi}{\partial r^2 \partial z} \tag{2.8a}$$

$$\sigma_{\theta\theta} = \lambda \nabla^2 \left(\frac{\partial \Phi}{\partial z}\right) - \frac{2(\lambda + \mu)}{r}\frac{\partial^2 \Phi}{\partial r \partial z} \tag{2.8b}$$

$$\sigma_{zz} = (3\lambda + 4\mu)\nabla^2 \left(\frac{\partial \Phi}{\partial z}\right) - 2(\lambda + \mu)\frac{\partial^3 \Phi}{\partial z^3} \tag{2.8c}$$

$$\sigma_{rz} = (\lambda + 2\mu)\frac{\partial}{\partial r}\left(\nabla^2 \Phi\right) - 2(\lambda + \mu)\frac{\partial^3 \Phi}{\partial z^2 \partial r} \tag{2.8d}$$

$$u_r = -\frac{\lambda+\mu}{\mu}\frac{\partial^2\Phi}{\partial r\partial z} \tag{2.8e}$$

$$u_z = \frac{\lambda+2\mu}{\mu}\nabla^2\Phi - \frac{\lambda+\mu}{\mu}\frac{\partial^2\Phi}{\partial z^2} \tag{2.8f}$$

By applying Hankel integral transforms, the biharmonic equation (2.7) can be reduced to

$$\left(\frac{d^2}{dz^2}-\xi^2\right)^2 G(\xi,z) = 0 \tag{2.9}$$

where $G(\xi,z)=\int_0^\infty r\Phi J_0(\xi r)\,dr$ and $J_n(\xi)$ denotes the first order Bessel functions of order n. The general solution of (2.9) is given by

$$G(\xi,z) = (A+Bz)e^{-\xi z}+(C+Dz)e^{\xi z} \tag{2.10}$$

where A, B, C and D are arbitrary functions of ξ that can be determined from boundary conditions.

Accordingly, the general solution for displacements and stresses can be transformed into the relations involving $G(\xi,z)$ and its derivatives with respect to z by using Hankel inversion and the relations (2.8a)-(2.8f):

$$\sigma_{rr} = \int_0^\infty \xi\left[\lambda\frac{d^3G}{dz^3}+(\lambda+2\mu)\xi^2\frac{dG}{dz}\right]J_0(\xi r)\,d\xi - \frac{2(\lambda+\mu)}{r}\int_0^\infty \xi^2\frac{dG}{dz}J_1(\xi r)\,d\xi \tag{2.11a}$$

$$\sigma_{\theta\theta} = \lambda\int_0^\infty \xi\left[\frac{d^3G}{dz^3}-\xi^2\frac{dG}{dz}\right]J_0(\xi r)\,d\xi + \frac{2(\lambda+\mu)}{r}\int_0^\infty \xi^2\frac{dG}{dz}J_1(\xi r)\,d\xi \tag{2.11b}$$

$$\sigma_{zz} = \int_0^\infty \xi\left[(\lambda+2\mu)\frac{d^3G}{dz^3}-(3\lambda+4\mu)\xi^2\frac{dG}{dz}\right]J_0(\xi r)\,d\xi \tag{2.11c}$$

$$\sigma_{rz} = \int_0^\infty \xi^2 \left[\lambda \frac{d^2 G}{dz^2} + (\lambda + 2\mu)\xi^2 G \right] J_1(\xi r)\, d\xi \tag{2.11d}$$

$$u_r = \frac{\lambda + \mu}{\mu} \int_0^\infty \xi^2 \frac{dG}{dz} J_1(\xi r)\, d\xi \tag{2.11e}$$

$$u_z = \int_0^\infty \xi \left[\frac{d^2 G}{dz^2} - \frac{\lambda + 2\mu}{\mu}\xi^2 G \right] J_0(\xi r)\, d\xi \tag{2.11f}$$

Note that u_θ, $\sigma_{r\theta}$ and $\sigma_{z\theta}$ vanish due to the axisymmetry and all non-zero field variables are independent of θ.

By invoking the remote condition associated with the vanishing displacements and stresses as $z \to \infty$, C and D must vanish and the function $G(\xi, z)$ therefore reduces to

$$G(\xi, z) = (A + Bz)e^{-\xi z} \tag{2.12}$$

Upon substituting (2.12) into (2.11), the expression for the components of stresses and displacements are then given in terms of A and B by

$$\frac{\sigma_{rr}}{2(\lambda + \mu)} = \int_0^\infty \xi^3 \left[-\xi A + \left(\frac{2\lambda + \mu}{\lambda + \mu} - \xi z \right) B \right] e^{-\xi z} J_0(\xi r)\, d\xi$$
$$- \frac{1}{r} \int_0^\infty \xi^2 \left[-\xi A + (1 - \xi z) B \right] e^{-\xi z} J_1(\xi r)\, d\xi \tag{2.13}$$

$$\frac{\sigma_{\theta\theta}}{2(\lambda + \mu)} = \frac{\lambda}{\lambda + \mu} \int_0^\infty \xi^3 B e^{-\xi z} J_0(\xi r)\, d\xi$$
$$+ \frac{1}{r} \int_0^\infty \xi^2 \left[-\xi A + (1 - \xi z) B \right] e^{-\xi z} J_1(\xi r)\, d\xi \tag{2.14}$$

$$\frac{\sigma_{zz}}{2(\lambda + \mu)} = \int_0^\infty \xi^3 \left[\xi A + \left(\frac{\mu}{\lambda + \mu} + \xi z \right) B \right] e^{-\xi z} J_0(\xi r)\, d\xi \tag{2.15}$$

$$\frac{\sigma_{rz}}{2(\lambda+\mu)} = \int_0^\infty \xi^3 \left[\xi A - \left(\frac{\lambda}{\lambda+\mu} - \xi z \right) B \right] e^{-\xi z} J_1(\xi r) d\xi \tag{2.16}$$

$$u_r = \frac{\lambda+\mu}{\mu} \int_0^\infty \xi^2 \left[-\xi A + (1-\xi z) B \right] e^{-\xi z} J_1(\xi r) d\xi \tag{2.17}$$

$$u_z = -\frac{\lambda+\mu}{\mu} \int_0^\infty \xi^2 \left[\xi A + \left(\frac{2\mu}{\lambda+\mu} + \xi z \right) B \right] e^{-\xi z} J_0(\xi r) d\xi \tag{2.18}$$

For the indentation problem shown in Figure 2.1, the boundary of the domain can be decomposed into a surface outside the contact region on which the traction identically vanishes and a surface inside the contact region on which the normal displacement is prescribed while, resulting from the frictionless assumption, the shear traction vanishes. These mixed boundary conditions can be expressed as

$$u_z \big|_{z=0} = d - \delta(r) \qquad\qquad ; \quad 0 \le r \le a \tag{2.19}$$

$$\sigma_{zz} \big|_{z=0} + \tau^s \nabla^2 u_z = 0 \qquad\qquad ; \quad a < r < \infty \tag{2.20}$$

$$\sigma_{rz} \big|_{z=0} + \kappa^s \left(\frac{d^2 u_r}{dr^2} + \frac{1}{r}\frac{du_r}{dr} - \frac{u_r}{r^2} \right)_{z=0} = 0 \qquad ; \quad 0 \le r < \infty \tag{2.21}$$

where $\kappa^s = 2\mu^s + \lambda^s$ is a surface material constant. Upon substituting (2.16) and (2.17) into the boundary condition (2.21), it leads to a relation between A and B:

$$A\xi(1+\Lambda_0\xi) = \left(\frac{\lambda}{\lambda+\mu} + \Lambda_0\xi \right) B \tag{2.22}$$

where $\Lambda_0 = \kappa^s / 2\mu$. By enforcing the mixed boundary conditions (2.19) and (2.20) along with the relation (2.22), it yields a pair of integral equations:

$$-\int_0^\infty \xi^2 \left[\frac{(\lambda+2\mu)+(\lambda+3\mu)\Lambda_0\xi}{\mu(1+\Lambda_0\xi)} \right] B J_0(\xi r) d\xi = d - \delta(r) \qquad ; \quad 0 \le r \le a \tag{2.23}$$

$$\int_0^\infty \xi^3 \left\{ \frac{2\mu\left[(\lambda+\mu)+(\lambda+2\mu)\Lambda_0\xi\right]+\tau^s\xi\left[(\lambda+2\mu)+(\lambda+3\mu)\Lambda_0\xi\right]}{\mu^2(1+\Lambda_0\xi)} \right\} BJ_0(\xi r)\,d\xi = 0$$

$$; \quad a < r < \infty \quad (2.24)$$

The dual integral equations (2.23) and (2.24) constitute a complete set of equations for determining the unknown function $B = B(\xi)$. By introducing two functions $\phi = \phi(\xi)$ and $w = w(\xi)$ such that

$$\phi(\xi) = \xi^3 \left\{ \frac{2\mu\left[(\lambda+\mu)+(\lambda+2\mu)\Lambda_0\xi\right]+\tau^s\xi\left[(\lambda+2\mu)+(\lambda+3\mu)\Lambda_0\xi\right]}{\mu^2(1+\Lambda_0\xi)} \right\} B \quad (2.25)$$

$$\xi^{-1}\phi(\xi)\left[1+w(\xi)\right] = \xi^2 \left[\frac{(\lambda+2\mu)+(\lambda+3\mu)\Lambda_0\xi}{\mu(1+\Lambda_0\xi)} \right] B \quad (2.26)$$

the dual integral equations (2.23) and (2.24) can further be simplified to

$$\int_0^\infty \overline{\xi}^{-1}\overline{\phi}(\overline{\xi})\left[1+w(\overline{\xi})\right]J_0(\overline{\xi}\overline{r})\,d\overline{\xi} = \overline{f}(\overline{r}) \qquad ; \quad 0 \le \overline{r} \le 1 \quad (2.27)$$

$$\int_0^\infty \overline{\phi}(\overline{\xi})J_0(\overline{\xi}\overline{r})\,d\overline{\xi} = 0 \qquad ; \quad 1 < \overline{r} < \infty \quad (2.28)$$

where $\overline{f}(\overline{r}) = f(\overline{r})/a = -[\overline{d}-\overline{\delta}(\overline{r})]$, $\overline{\delta}(\overline{r}) = \delta(\overline{r})/a$, $\overline{d} = d/a$, $\overline{\xi} = \xi a$, $\overline{r} = r/a$, and $\overline{\phi} = \overline{\phi}(\overline{\xi}) = \phi(\overline{\xi})/a$. The function $\overline{\phi} = \overline{\phi}(\overline{\xi})$ becomes the primary unknown of the dual integrals (2.27) and (2.28) while the function $w = w(\overline{\xi})$ is known and can be obtained directly from (2.25) and (2.26) as

$$w(\overline{\xi}) = \frac{(\overline{\lambda}+2)+(\overline{\lambda}+3)\overline{\Lambda}_0\overline{\xi}}{2\left[(\overline{\lambda}+1)+(\overline{\lambda}+2)\overline{\Lambda}_0\overline{\xi}\right]+\overline{\tau}^s\overline{\xi}\left[(\overline{\lambda}+2)+(\overline{\lambda}+3)\overline{\Lambda}_0\overline{\xi}\right]} - 1 \quad (2.29)$$

where $\overline{\lambda} = \lambda/\mu$, $\overline{\Lambda}_0 = \Lambda_0/a$ and $\overline{\tau}^s = \tau^s/(\mu a)$. It is evident from (2.29) that the function $w = w(\overline{\xi})$ possesses a limit equal to -1 as $\overline{\xi} \to \infty$.

The solution of dual integral equations of the type (2.27) and (2.28) has been extensively studied by Mandal (1988) and Sneddon (1966). Following their procedures, such a set of dual integral equations can be reduced to a Fredholm integral equation of the second kind as

$$\bar{\phi}\left(\bar{\bar{\xi}}\right) = \frac{2\bar{\bar{\xi}}}{\pi}\int_0^1 \cos\left(\bar{\bar{\xi}}t\right)dt\,\frac{d}{dt}\int_0^t \frac{uf(u)\,du}{\sqrt{t^2-u^2}} - \frac{\bar{\bar{\xi}}}{\pi}\int_0^\infty \frac{w(u)\bar{\phi}(u)}{u}\left\{\frac{\sin\left(u+\bar{\bar{\xi}}\right)}{u+\bar{\bar{\xi}}} + \frac{\sin\left(u-\bar{\bar{\xi}}\right)}{u-\bar{\bar{\xi}}}\right\}du \quad (2.30)$$

It can be seen from (2.30) that the function $f(u)$ is merely related to the indenter profile and the function $w(u)$ is related to the boundary conditions involving the surface energy parameters. This single integral equation (2.30) is in a form well-suited for constructing numerical solutions for $\bar{\phi} = \bar{\phi}\left(\bar{\bar{\xi}}\right)$. Once the function $\bar{\phi} = \bar{\phi}\left(\bar{\bar{\xi}}\right)$ is solved, the functions A and B can be subsequently determined from (2.22) and (2.25), respectively, and the complete elastic fields within the half-space can also be obtained from (2.13)-(2.18). In addition, the magnitude of the total indentation force P producing the indentation depth d can be obtained by integrating the contact pressure, i.e. the left hand side of Eq. (2.20), over the area of the contact region.

In the absence of surface energy effects, above formulation can readily be specialized to a special case of a classical indentation problem by setting $\bar{\Lambda}_0 = 0$ and $\bar{\tau}^s = 0$. The function $w = w\left(\bar{\bar{\xi}}\right)$ in (2.29) simply reduces to a constant w^* given below:

$$w^* = \frac{\bar{\lambda}+2}{2\left(\bar{\lambda}+1\right)} - 1 \quad (2.31)$$

The dual integral equations (2.23) and (2.24) now become

$$\int_0^\infty \bar{\bar{\xi}}^{-1}\bar{\phi}\left(\bar{\bar{\xi}}\right)J_0\left(\bar{\bar{\xi}}\bar{r}\right)d\bar{\bar{\xi}} = f^*(\bar{r}) \qquad\qquad ;\quad 0 \le \bar{r} \le 1 \quad (2.32)$$

$$\int_0^\infty \overline{\phi}\left(\overline{\xi}\right) J_0\left(\overline{\xi}\,\overline{r}\right) d\overline{\xi} = 0 \qquad\qquad ;\quad 1 < \overline{r} < \infty \qquad (2.33)$$

where $f^*\left(\overline{r}\right) = \overline{f}\left(\overline{r}\right)/w^*$. A set of dual integral equations (2.32) and (2.33) was solved analytically by Sneddon (1965).

ศูนย์วิทยทรัพยากร
จุฬาลงกรณ์มหาวิทยาลัย

CHAPTER III

NUMERICAL IMPLEMENTATIONS

Due to the complexity of the Fredholm integral equation of the second kind formulated in Chapter II, numerical schemes are necessarily adopted to construct approximate solutions. In this chapter, several components essential for such numerical implementation (e.g. domain truncation, discretization of the primary unknown function $\bar{\phi} = \bar{\phi}(\bar{\xi})$, collocation, linear solvers, Hankel transform inversion, etc.) are briefly summarized.

3.1 Domain Truncation

It is evident that the second integral of the Fredholm integral equation (2.30) is an improper integral with an infinite upper limit and the involved primary unknown function $\bar{\phi} = \bar{\phi}(\bar{\xi})$ is defined on a semi-infinite interval $[0, \infty)$. Before constructing an approximate solution for $\bar{\phi} = \bar{\phi}(\bar{\xi})$, the domain of integration of the improper integral is first truncated from $[0, \infty)$ to $[0, \bar{\xi}_R]$ where $\bar{\xi}_R$ is a finite real number. The truncated Fredholm integral equation is given by

$$\bar{\phi}(\bar{\xi}) = \frac{2\bar{\xi}}{\pi} \int_0^1 \cos(\bar{\xi}t)dt \frac{d}{dt} \int_0^t \frac{uf(u)du}{\sqrt{t^2 - u^2}} - \frac{\bar{\xi}}{\pi} \int_0^{\bar{\xi}_R} \frac{w(u)\bar{\phi}(u)}{u} \left\{ \frac{\sin(u+\bar{\xi})}{u+\bar{\xi}} + \frac{\sin(u-\bar{\xi})}{u-\bar{\xi}} \right\} du \quad (3.1)$$

3.2 Discretization

The unknown function $\bar{\phi} = \bar{\phi}(\bar{\xi})$ over the entire truncated domain $[0, \bar{\xi}_R]$ can be discretized in the form

$$\bar{\phi}(\bar{\xi}) = \bar{\xi} \sum_{j=1}^n \alpha_j \psi_j(\bar{\xi}) \qquad (3.2)$$

where α_j are unknown nodal quantities to be determined, $\psi_j(\xi)$ are nodal basis functions, and n is the number of nodes resulting from the discretization. It is worth noting that the approximation (3.2) results from a special property of the function ϕ at the origin; more specifically, this function vanishes at the origin of order $\mathcal{O}(\bar{\xi})$. Note also that, in the present study, the nodal basis functions are systematically constructed in an element-wise fashion based on standard isoparametric, quadratic elements.

Upon inserting the approximation (3.2) into (3.1) and then dividing the entire equation by $\bar{\xi}$, it leads to a discretized integral equation

$$\sum_{j=1}^{n} \mathcal{M}_j(\bar{\xi})\alpha_j = \mathcal{F}(\bar{\xi}) \tag{3.3}$$

where the integrals $\mathcal{M}_j(\bar{\xi})$ and $\mathcal{F}(\bar{\xi})$ are defined on the truncated domain $[0, \xi_R]$ by

$$\mathcal{M}_j(\bar{\xi}) = \psi_j(\bar{\xi}) + \int_0^{\bar{\xi}_R} \psi_j(u) K(\bar{\xi}, u) du \tag{3.4}$$

$$\mathcal{F}(\bar{\xi}) = \frac{2}{\pi} \int_0^1 \cos(\bar{\xi}t) dt \frac{d}{dt} \int_0^t \frac{uf(u)du}{\sqrt{t^2 - u^2}} \tag{3.5}$$

$$K(\bar{\xi}, u) = \frac{w(u)}{\pi} \left\{ \frac{\sin(u + \bar{\xi})}{u + \bar{\xi}} + \frac{\sin(u - \bar{\xi})}{u - \bar{\xi}} \right\} \tag{3.6}$$

It can readily be verified that the kernel $K(\bar{\xi}, u)$ is regular for any pair of points ($\bar{\xi}$, u) and, as a result, $\mathcal{M}_j(\bar{\xi})$ involves only an regular integral for all $\bar{\xi} \in [0, \bar{\xi}_R]$. The integral $\mathcal{F}(\bar{\xi})$ is given in terms of a double line integral whose inner integrand involves the prescribed profile of the punch and is only weakly singular at $u = t$. To obtain a better form well-suited for numerical integration, an integration by parts is performed along with applying a special variable transformation (i.e. $u = t\sin\theta$) to remove such singularity and this, finally, leads to

$$\mathcal{F}(\bar{\xi}) = \frac{2\bar{\xi}}{\pi}\int_0^1 \sin(\bar{\xi}t)\int_0^{\pi/2} uf(u)\big|_{u=t\sin\theta}\,d\theta dt + \frac{2\cos(\bar{\xi})}{\pi}\int_0^{\pi/2} uf(u)\big|_{u=\sin\theta}\,d\theta \tag{3.7}$$

3.3 Collocation Method

To obtain a sufficient number of equations to solve for the unknown constants α_j, a collocation-based technique is utilized. In particular, the discretized integral equation (3.3) is collocated (or, equivalent, forced to be satisfied) at all nodes $\bar{\xi} = \bar{\xi}_i$ (for $i = 1, 2, 3, ..., n$) and this leads to a set of n linear algebraic equations governing the nodal quantities α_j as follows

$$\mathbf{M}\boldsymbol{\alpha} = \mathbf{F} \tag{3.8}$$

where $\boldsymbol{\alpha} = \{\alpha_1, \alpha_2, ..., \alpha_n\}^T$ is vector of nodal quantities and entries of the coefficient matrix $\mathbf{M}$ and the prescribed vector $\mathbf{F}$ are given by

$$[\mathbf{M}]_{ij} = \mathcal{M}_j(\bar{\xi}_i) = \psi_j(\bar{\xi}_i) + \int_0^{\bar{\xi}_R} \psi_j(u)K(\bar{\xi}_i, u)du \tag{3.9}$$

$$[\mathbf{F}]_i = \mathcal{F}(\bar{\xi}_i) = \frac{2\bar{\xi}_i}{\pi}\int_0^1 \sin(\bar{\xi}_i t)\int_0^{\pi/2} uf(u)\big|_{u=t\sin\theta}\,d\theta dt + \frac{2\cos(\bar{\xi}_i)}{\pi}\int_0^{\pi/2} uf(u)\big|_{u=\sin\theta}\,d\theta \tag{3.10}$$

3.4 Construction of M and F

It is evident from (3.9) and (3.10) that entries of the matrix $\mathbf{M}$ and the prescribed vector $\mathbf{F}$ involve only regular integrals. Thus, a standard Gaussian quadrature can be used to efficiently and accurately evaluate such integrals. While every entry of the matrix $\mathbf{M}$ is given in terms of a definite integral over the truncated domain [0, $\bar{\xi}_R$], this matrix can be efficiently constructed in an element-wise fashion and the contribution from all elements to the global matrix $\mathbf{M}$ can readily be treated using a standard assembly procedure (e.g. Hughes, 2000). It is worth noting that for some special punch profiles, the integral $\mathcal{F}(\bar{\xi})$ admits an explicit expression and, as a result, construction of the corresponding vector $\mathbf{F}$ requires no numerical integration.

For instance, the integral $\mathcal{F}(\bar{\xi})$ can be obtained for a flat-ended cylindrical indenter (i.e. $\bar{\delta}(\bar{r}) = 0$) and a paraboloidal indenter (i.e. $\bar{\delta}(\bar{r}) = \alpha a \bar{r}^2$ where α is a constant representing the slenderness of the punch profile) as

Flat-ended cylindrical indenter: $\mathcal{F}(\bar{\xi}) = -\dfrac{2\bar{d}}{\pi\bar{\xi}}\sin(\bar{\xi})$ (3.11)

Paraboloidal indenter: $\mathcal{F}(\bar{\xi}) = -\dfrac{2\bar{d}}{\pi\bar{\xi}}\sin(\bar{\xi}) + \dfrac{4\alpha a}{\pi\bar{\xi}^3}\left\{2\bar{\xi}\cos(\bar{\xi}) + (-2+\bar{\xi}^2)\sin(\bar{\xi})\right\}$ (3.12)

3.5 Linear Solvers

It is evident from equation (3.9) that the coefficient matrix **M** is non-symmetric and fully dense. To solve a system of linear equations (3.8), either a direct solver based on the LU-decomposition method or an iterative solver adopted from the stabilized bi-conjugate gradient method is employed. Once the nodal quantities α_j are known, the approximate solution for $\bar{\phi} = \bar{\phi}(\bar{\xi})$ can readily be obtained from (3.2) for any $\bar{\xi}$ in the truncated domain $[0, \bar{\xi}_R]$.

3.6 Determination of Field Quantities

Once the numerical solution $\bar{\phi} = \bar{\phi}(\bar{\xi})$ is obtained, functions $\bar{A} = \bar{A}(\bar{\xi}) = A(\bar{\xi})/a^5$ and $\bar{B} = \bar{B}(\bar{\xi}) = B(\bar{\xi})/a^4$ can be obtained at any $\bar{\xi} \in [0, \bar{\xi}_R]$ by directly solving the relations (2.22) and (2.25) via proper normalization. The explicit formula for $\bar{A} = \bar{A}(\bar{\xi})$ and $\bar{B} = \bar{B}(\bar{\xi})$ in terms of $\bar{\phi} = \bar{\phi}(\bar{\xi})$ is given by

$$A(\bar{\xi}) = \frac{\left(\dfrac{\bar{\lambda}}{\bar{\lambda}+1} + \overline{\Lambda}_0\bar{\xi}\right)\bar{\phi}(\bar{\xi})}{\bar{\xi}^4\left\{2\left[(\bar{\lambda}+1) + (\bar{\lambda}+2)\overline{\Lambda}_0\bar{\xi}\right] + \overline{\tau}^s\bar{\xi}\left[(\bar{\lambda}+2) + (\bar{\lambda}+3)\overline{\Lambda}_0\bar{\xi}\right]\right\}}$$ (3.13)

$$B(\bar{\xi}) = \frac{\left(1 + \overline{\Lambda}_0\bar{\xi}\right)\bar{\phi}(\bar{\xi})}{\bar{\xi}^3\left\{2\left[(\bar{\lambda}+1) + (\bar{\lambda}+2)\overline{\Lambda}_0\bar{\xi}\right] + \overline{\tau}^s\bar{\xi}\left[(\bar{\lambda}+2) + (\bar{\lambda}+3)\overline{\Lambda}_0\bar{\xi}\right]\right\}}$$ (3.14)

The stress and displacement fields within the elastic half-space can then be obtained from the integrals (2.13)-(2.18) via proper normalization and with the upper limited being replaced by $\overline{\xi}_R$, i.e.

$$\overline{\sigma}_{rr}(\overline{r},\overline{z}) = \frac{\sigma_{rr}}{2(\lambda+\mu)} = \int_0^{\overline{\xi}_R} \overline{\xi}^3 \left[-\overline{\xi}\,\overline{A} + \left(\frac{2\overline{\lambda}+1}{\overline{\lambda}+1} - \overline{\xi}\,\overline{z} \right)\overline{B} \right] e^{-\overline{\xi}\,\overline{z}} J_0\left(\overline{\xi}\,\overline{r}\right) d\overline{\xi}$$

$$-\frac{1}{\overline{r}} \int_0^{\overline{\xi}_R} \overline{\xi}^2 \left[-\overline{\xi}\,\overline{A} + \left(1 - \overline{\xi}\,\overline{z}\right)\overline{B} \right] e^{-\overline{\xi}\,\overline{z}} J_1\left(\overline{\xi}\,\overline{r}\right) d\overline{\xi}$$

(3.15)

$$\overline{\sigma}_{\theta\theta}(\overline{r},\overline{z}) = \frac{\sigma_{\theta\theta}}{2(\lambda+\mu)} = \frac{\overline{\lambda}}{\overline{\lambda}+1} \int_0^{\overline{\xi}_R} \overline{\xi}^3 \overline{B} e^{-\overline{\xi}\,\overline{z}} J_0\left(\overline{\xi}\,\overline{r}\right) d\overline{\xi}$$

$$+\frac{1}{\overline{r}} \int_0^{\overline{\xi}_R} \overline{\xi}^2 \left[-\overline{\xi}\,\overline{A} + \left(1 - \overline{\xi}\,\overline{z}\right)\overline{B} \right] e^{-\overline{\xi}\,\overline{z}} J_1\left(\overline{\xi}\,\overline{r}\right) d\overline{\xi}$$

(3.16)

$$\overline{\sigma}_{zz}(\overline{r},\overline{z}) = \frac{\sigma_{zz}}{2(\lambda+\mu)} = \int_0^{\overline{\xi}_R} \overline{\xi}^3 \left[\overline{\xi}\,\overline{A} + \left(\frac{1}{\overline{\lambda}+1} + \overline{\xi}\,\overline{z} \right)\overline{B} \right] e^{-\overline{\xi}\,\overline{z}} J_0\left(\overline{\xi}\,\overline{r}\right) d\overline{\xi}$$

(3.17)

$$\overline{\sigma}_{rz}(\overline{r},\overline{z}) = \frac{\sigma_{rz}}{2(\lambda+\mu)} = \int_0^{\overline{\xi}_R} \overline{\xi}^3 \left[\overline{\xi}\,\overline{A} - \left(\frac{\overline{\lambda}}{\overline{\lambda}+1} - \overline{\xi}\,\overline{z} \right)\overline{B} \right] e^{-\overline{\xi}\,\overline{z}} J_1\left(\overline{\xi}\,\overline{r}\right) d\overline{\xi}$$

(3.18)

$$\overline{u}_r(\overline{r},\overline{z}) = \frac{u_r}{a} = (\overline{\lambda}+1) \int_0^{\overline{\xi}_R} \overline{\xi}^2 \left[-\overline{\xi}\,\overline{A} + \left(1 - \overline{\xi}\,\overline{z}\right)\overline{B} \right] e^{-\overline{\xi}\,\overline{z}} J_1\left(\overline{\xi}\,\overline{r}\right) d\overline{\xi}$$

(3.19)

$$\overline{u}_z(\overline{r},\overline{z}) = \frac{u_z}{a} = -(\overline{\lambda}+1) \int_0^{\overline{\xi}_R} \overline{\xi}^2 \left[\overline{\xi}\,\overline{A} + \left(\frac{2}{\overline{\lambda}+1} + \overline{\xi}\,\overline{z} \right)\overline{B} \right] e^{-\overline{\xi}\,\overline{z}} J_0\left(\overline{\xi}\,\overline{r}\right) d\overline{\xi}$$

(3.20)

where $\overline{z} = z/a$. To evaluate such truncated Hankel transform inversions for any pair of points $(\overline{r},\overline{z})$, standard Gaussian quadrature is again employed. It is important to point out that presence of the exponential term $e^{-\overline{\xi}\,\overline{z}}$ in the integrand significantly increases the rate of decay of the unfavorable oscillated behavior arising from the Bessel functions $J_n(\overline{\xi})$ for $\overline{z} > 0$ and, as a result, the associated integrals converges very rapidly with a relatively low $\overline{\xi}_R$. On the contrary, such exponential term

becomes one on a free surface of the half-space (i.e. $\bar{z} = 0$) and, due to the slow rate of decay of the Bessel functions, it generally requires a sufficiently large $\bar{\xi}_R$ for those integrals associated with $\bar{z} = 0$ to achieve their converged value.

Once the elastic fields within the half-space are obtained, other interesting quantities can also be computed. For instance, the normalized contact pressure under the punch, denoted by $\bar{p} = \bar{p}(\bar{r})$, can readily be obtained from

$$\bar{p}(\bar{r}) = \frac{p}{2(\lambda + \mu)} = -\left[\bar{\sigma}_{zz}(\bar{r}, \bar{z} = 0) + \frac{\bar{\tau}^s \nabla^2 \bar{u}_z(\bar{r}, \bar{z} = 0)}{2(\bar{\lambda} + 1)} \right] \quad ; \quad 0 \le \bar{r} < 1 \tag{3.21}$$

It is remarked that the Laplacian of the normal displacement appearing on the right hand side of (3.21) can directly be evaluated using the prescribed boundary condition (2.19). The normalized indentation force $\bar{P}$ can further be computed by integrating the contact pressure $\bar{p} = \bar{p}(\bar{r})$ over the contact region:

$$\bar{P} = \frac{P}{2a^2(\lambda + \mu)} = -\int_0^{2\pi} \int_0^1 \bar{p}(\bar{r}) \bar{r} d\bar{r} d\theta = -2\pi \int_0^1 \bar{p}(\bar{r}) \bar{r} d\bar{r} \tag{3.22}$$

3.7 Determination of Contact Radius *a* for Smooth-contact Punch

For a smooth-contact punch, the contact radius *a* is unknown a priori and must be determined first before other quantities of interest can be obtained. It is remarked first that once the contact radius *a* is known, there is no difference of a solution procedure for both smooth-contact and nonsmooth-contact punch. To solve for a final contact region *a* that corresponds to a given indentation depth *d*, a physically admissible condition associated with the continuity of the vertical stress at $r = a$ is utilized. However, the explicit or close-form relationship between those two parameters (*a* and *d*) cannot be obtained due to the complexity of the boundary value problem accounted for the surface energy effects.

3.8 Convergence Study

For the proposed numerical technique, three key factors that affect the accuracy of the approximate solutions are the truncation parameter $\bar{\bar{\xi}}_R$, the number of elements employed in the discretization, and the number of integration points used in standard Gaussian quadrature. Extensive numerical experiments have been performed to choose a proper truncated domain, the level of mesh refinement and optimal quadrature to ensure the convergence and accuracy of numerical results. Such investigation is briefly discussed below.

The number of Gauss points required in the numerical integration can be significant to accurately integrate oscillating and complex integrands (resulting from the Bessel functions, $\bar{\phi} = \bar{\phi}(\bar{\xi})$, the kernel $K(\bar{\bar{\xi}}, u)$). From numerical experiments, it is found that as the size of elements decreases (i.e. the number of elements in the discretization increases), it only requires few Gauss points to achieve highly accurate results since the integrand on each element exhibits milder variation without oscillating behavior.

To investigate the level of mesh refinement required to obtain the converged results, we perform experiments for a given truncated domain $[0, \bar{\bar{\xi}}_R]$. A series of meshes on the fixed $[0, \bar{\bar{\xi}}_R]$ is constructed and then used in the analysis. The number of elements (N) in the discretization is increased until a converged solution (for a specified tolerance) is obtained for a fixed $\bar{\bar{\xi}}_R$. By repeating the analysis for various $\bar{\bar{\xi}}_R$, a ratio $N/\bar{\bar{\xi}}_R$ (representing the level of mesh refinement) to ensure the good discretization is found approximately equal to 1.

To obtain a proper truncated domain that optimizes the computational cost but, at the same time, yields accurate results, we next investigate the convergence of approximate solutions with respect to the truncated parameter $\bar{\bar{\xi}}_R$. From such study, it can be concluded that the truncated parameter $\bar{\bar{\xi}}_R$ to attain a converged results for the non-smooth contact punch is much larger than that for the smooth contact punch. This

is due primarily to the singularity induced at the boundary of the contact region of the non-smooth contact punch. Suggested by various experiments, the truncated parameter $\overline{\xi}_R$ in the analysis of non-smooth contact and smooth contact punches equal to 10,000 and 1,000, respectively.

CHAPTER IV

NUMERICAL RESULTS

The solution procedure described in chapter III is implemented as an in-house computer code to determine the complete elastic fields for punches of both smooth and non-smooth contacts. The accuracy of the present numerical scheme is first verified by comparing with analytical solutions of the classical case (no surface energy effects) for both categories. Once the method is tested, it is then applied to solve more complex indentation problems accounted for surface stress effects in which analytical solutions do not exist. In the analysis, punches with flat-ended and paraboloidal profiles are chosen to represent the non-smooth and smooth contacts, respectively. Numerical results for three different models (i.e. classical solution with no surface stress effects and solutions accounted for surface stress effects with and without the out-of-plane contribution of the residual surface tension) are fully compared and discussed.

4.1 Verification with Analytical Solutions

Consider a rigid frictionless punch with a flat-ended cylindrical profile (i.e. $\delta(r) = 0$) and a paraboloidal profile (i.e. $\delta(r) = \alpha\, r^2$ where α is a constant) indented on an isotropic, elastic half-space as shown schematically in Figure 4.1(a) and Figure 4.1(b), respectively. Note that, for both punch profiles, the total indentation depth at the tip of the punch d and the final radius of contact a are associated with the total indentation force P. With no surface surface effect, the analytical solutions derived by Sneddon (1965) are employed to validate the proposed formulation and numerical implementations. In numerical experiments, the present solution scheme is specialized to treat the classical case by setting $\overline{\Lambda}_0 = 0$ and $\overline{\tau^s} = 0$. According to Sneddon (1965), the distribution of contact pressure under the punch p_c, the shape of the deformed boundary $u_z(r, 0)$ and the total indentation force P_c required to produce the indentation depth d for flat-ended cylindrical and paraboloidal punches are summarized below.
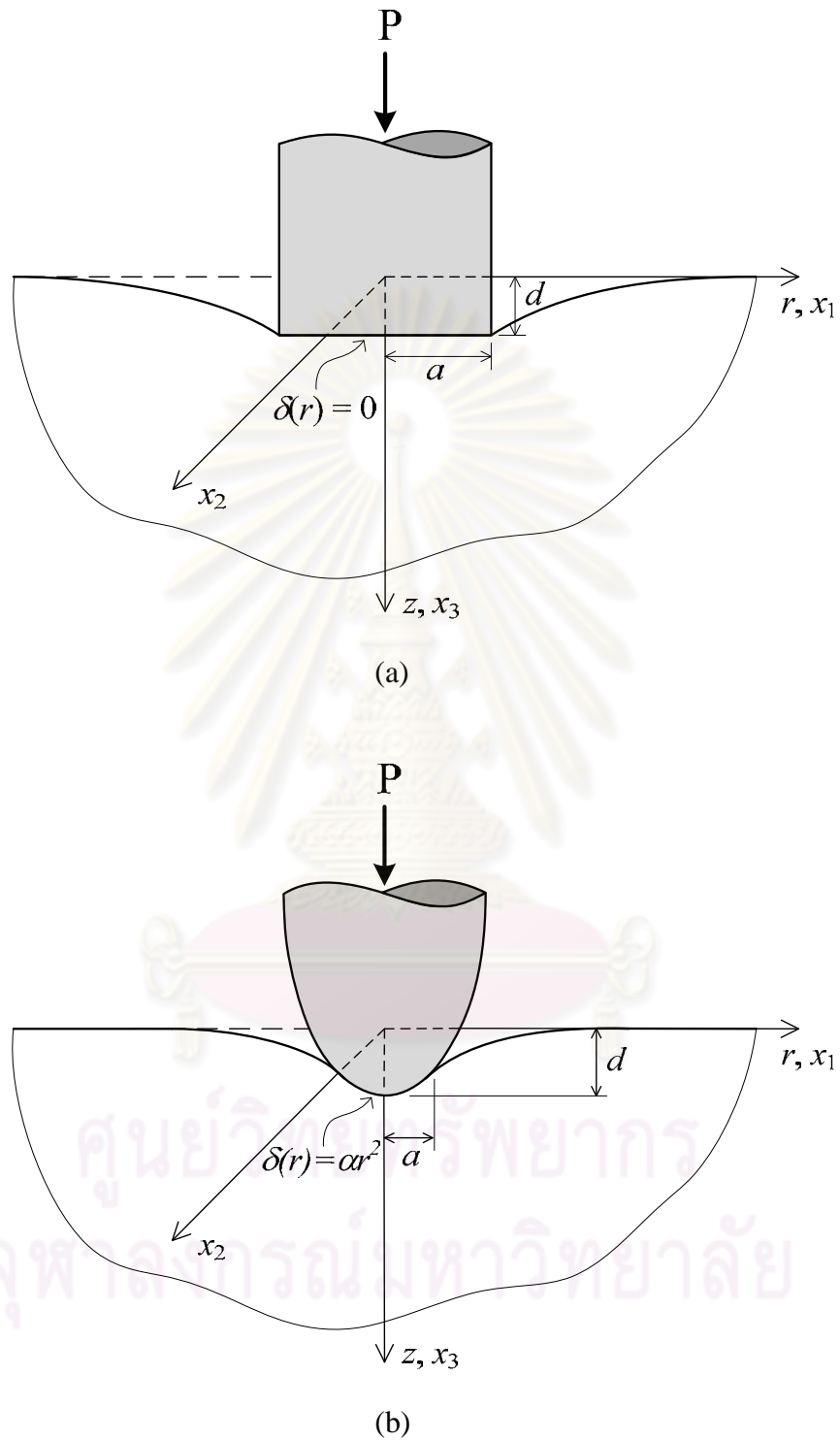
Figure 4.1 Indentation of half-space by axisymmetric rigid frictionless punch:

(a) flat-ended cylindrical punch and (b) paraboloidal punch

(a) Flat-ended Cylindrical Punch

$$p_c = \frac{4\mu(\lambda+\mu)d}{\pi(\lambda+2\mu)a}\frac{1}{\sqrt{1-(r/a)^2}} \qquad\qquad ; \quad 0 \le r < a \qquad (4.1)$$

$$u_z(r,0) = \frac{2d}{\pi}\sin^{-1}(a/r) \qquad\qquad ; \quad r > a \qquad (4.2)$$

$$P_c = \frac{8\mu(\lambda+\mu)}{\lambda+2\mu}ad \qquad\qquad (4.3)$$

(b) Paraboloidal Punch

$$a_c^{\,2} = \frac{d}{2\alpha} \qquad\qquad (4.4)$$

$$p_c = \frac{8\mu(\lambda+\mu)d}{\pi a(\lambda+2\mu)}\sqrt{1-(r/a)^2} \qquad\qquad ; \quad 0 \le r < a \qquad (4.5)$$

$$u_z(r,0) = \frac{d}{\pi}\left\{(2-(r/a)^2)\sin^{-1}(a/r)+\frac{r}{a}\sqrt{1-(a/r)^2}\right\} \qquad ; \quad r > a \qquad (4.6)$$

$$P_c = \frac{32\mu(\lambda+\mu)}{3(\lambda+2\mu)}\alpha a^3, \qquad\qquad (4.7)$$

Though the properties of elastic materials in the present study can be arbitrary, to simply compare some elastic quantities with those obtained by Zhao (2009), the same set of material properties is uitilized. Aluminum is used for the bulk material (Meyers and Chawla, 1999) whereas Al [1 1 1] is employed for the surface (Miller and Shenoy, 2000); all material constants are summarized in Table 4.1. In the numerical study, it is convenient to introduce following non-dimensional quantities: $r_0 = r/\Lambda_0$; $z_0 = z/\Lambda_0$; $a_0 = a/\Lambda_0$; $d_0 = d/\Lambda_0$ and $\alpha_0 = \alpha\,\Lambda_0$. It is worth noting that although the classical solution is independent of Λ_0, use of this parameter in the non-dimensionalization allows a direct comparison between non-classical and classical solutions.

In the case of flat-ended cylindrical punch with contact radius $a_0 = 0.5$, comparisons betwen numerical solutions for the classical contact pressure and classical vertical displacement and the benchmark solutions are reported in Figure 4.2(a) and Figure 4.2(b), respectively. It is evidently found that numerical results obtained from the present study are almost indistinguishable from the exact solutions proposed by Sneddon (1965). Another comparison is performed for the case of paraboloidal punch with $\alpha_0 = 0.5$. It can be obviously seen from Figure 4.3(a) and Figure 4.3(b) that two numerical solutions obtained from the present scheme, one is the contact pressure and the other is the vertical displacement at the free surface, again exhibit excellent agreement with the corresponding analytical solutions. This additionally confirms the accuracy of the present technique.

4.2 Results of Punch with Surface Stress Effects

From the high accuracy of numerical solutions obtained for the classical case, the proposed scheme is now convincingly applied to investigate the indentation problems with the surface stress effects being incorporated. To allow comparisons with results obtained from Zhao (2009) and demonstrate the significant role of the surface residual tension τ^s, Gurtin-Murdoch model without the out-of-plane contribution of τ^s is also considered. Selected numerical results are reported and dicussed for both punch profiles as follows.

4.2.1 Flat-ended Cylindrical Punch

The case of a flat-ended cylindrical punch indented on the half-space with a specified contact radius a and indentation depth d shown in Figure 4.1(a) is first examined. Note that this punch is an example of a non-smooth contact punch since $d\delta/dr$ is not well-defined at $r = a$. The corresponding elastic fields within the half-space are reported in Figures 4.4-4.7.

It can be obviously seen from Figure 4.4 that the distribution of the contact pressure under the punch accounted for the surface effects possesses the same trend as that for the classical solution in which the singularity still exists at the boundary of the

punch. Due to the integration of the out-of-plane contribution of the surface tension, the predicted contact pressure for this particular model is considerably less than one obtained from the other two models (e.g. the classical model and Gurtin-Murdoch model without the out-of-plane contribution of τ^s). In the analysis, three values of the contact radii, $a_0 = 0.5$, 1.0 and 1.5, are considered to study the size-dependent behavior and found that when the radius of a punch is smaller and in the same order as Λ_0, the effects of surface stresses are comparatively larger. It is interesting to point out that when the contact pressure p has been normalized in a proper manner (i.e. normalized as $\pi p a_0 / 4\mu d_0$), size-dependent behavior due to the influence of surface energy effects is significantly demonstrated and this phenomenon cannot be certainly observed in the classical model (only one single dotted line is shown in spite of changing the contact radius a_0). It implies that the classical model ignores an inevitable material parameter (i.e. the intrinsic length Λ_0) and, as a result, it predicts erroneous solutions when the radius of a punch is very small. However, the contact pressure under the larger punch (i.e. larger contact radius a_0) for both models accounted for the surface energy effects converges monotonically to the classical solution.

The variations of normalized vertical stresses, $\pi \sigma_{zz}/4\mu d_0$, along the radial direction at four depths, $z_0 = 0.1$, 0.5, 1.0 and 1.5, with contact radius $a_0 = 0.5$ are shown in Figure 4.5. The vertical stress profiles indicate the strong influence of the surface energy effects for region relatively closed to the punch. In particular, at very small depth (i.e. $z_0 = 0.1$), the vertical stress increases monotonically and reaches their peak values near $r_0/a_0 = 1$ and then starts to drop rapidly when r_0 increases. At larger depths, the vertical stress reaches its maximum at $r_0 = 0$ and decreases monotonically to zero at relatively large r_0. It is evident that an ideal surface attached to the bulk of the current model distributes the localized indentation force to an area outside the contact region. As a direct consequence, the current model (i.e. Gurtin-Murdoch model with the out-of-plane contribution of τ^s) predicts the lower vertical stress under the punch and higher vertical stress outside the contact region than those obtained from the other two models. However, such discrepancy becomes insignificant in the region far away from the punch.

Numerical results of normalized shear stresses, $\pi\sigma_{rz}/4\mu d_0$, and radial stresses, $\pi\sigma_{rr}/4\mu d_0$, at various depths with contact radius $a_0 = 0.5$ are also presented in Figure 4.6(a) and Figure 4.6(b), respectively. Similar to the vertical stresses, the magnitudes of shear stresses along the radial direction predicted by the current model are generally lower and higher than those obtained from the other two models for regions inside and outside the contact, respectively. The shear stress at any depth vanishes at $r_0 = 0$ because of the axisymmetry and it reaches its peak value near the edge of the punch ($r_0/a_0 = 1$) and, thereafter, decreases rapidly with r_0. However, such behavior is not observed for the radial stress; for instance, the magnitude of radial stress at $z_0 = 0.5$ obtained from the current model lies between those predicted by the other two models for a region inside the contact. As expected, the shear and radial stresses obtained from all three models for relatively large r_0 possess the same trend and decay monotonically to zero. The inflence of surface energy effects is extremely small for $z_0 \geq 1.5$ as clearly demonstrated by insignificant discrepancy between solutions obtained from the current and classical models.

According to results shown in Figure 4.7(a) for the normalized vertical displacement, $u_z/\Lambda_0 d_0$, along the radial direction at five depths, $z_0 = 0.0, 0.1, 0.5, 1.0$ and 1.5, with contact radius $a_0 = 0.5$, one predicted by the current model is comparatively higher than those obtained from the other two models due to the need of higher indentation force to produce the same indentation depth. Unlike the stress solutions, vertical displacements exhibit a slower decay rate as z_0 increases while they still gradually converge to the classical solutions. As the final illustration of elastic fields for this particular punch, the normalized radial displacement, $u_r/\Lambda_0 d_0$, at four dfifferent depths, $z_0 = 0.1, 0.5, 1.0$ and 1.5, with the same contact radius $a_0 = 0.5$ is reported in Figure 4.7(b). Clearly, the radial displacement increases rapidly from zero at $r_0 = 0$ to its peak value at relatively small r_0 and then gradually decreases with r_0. It should be noted that the surface energy effects only influence the magnitude of the radial displacement while its distribution along the radial direction predicted by all three models is quite similar.
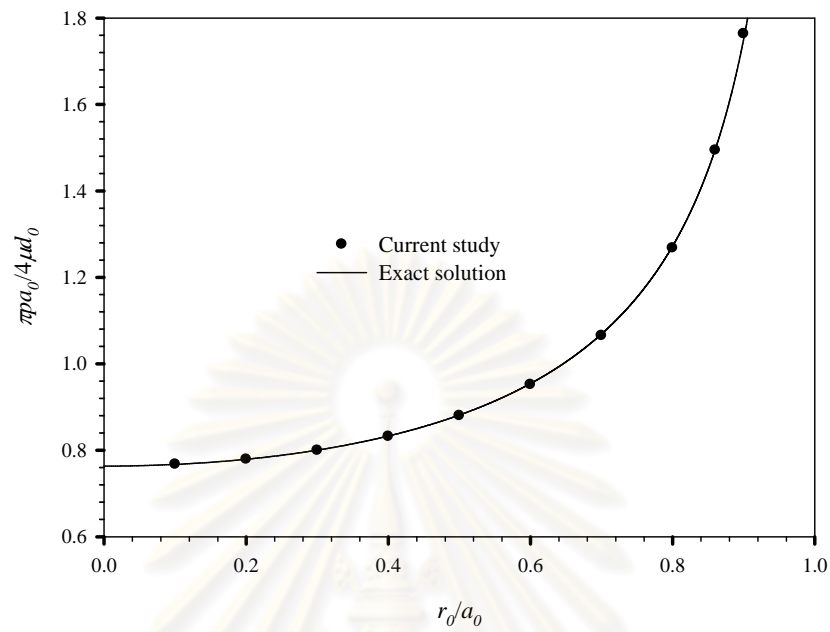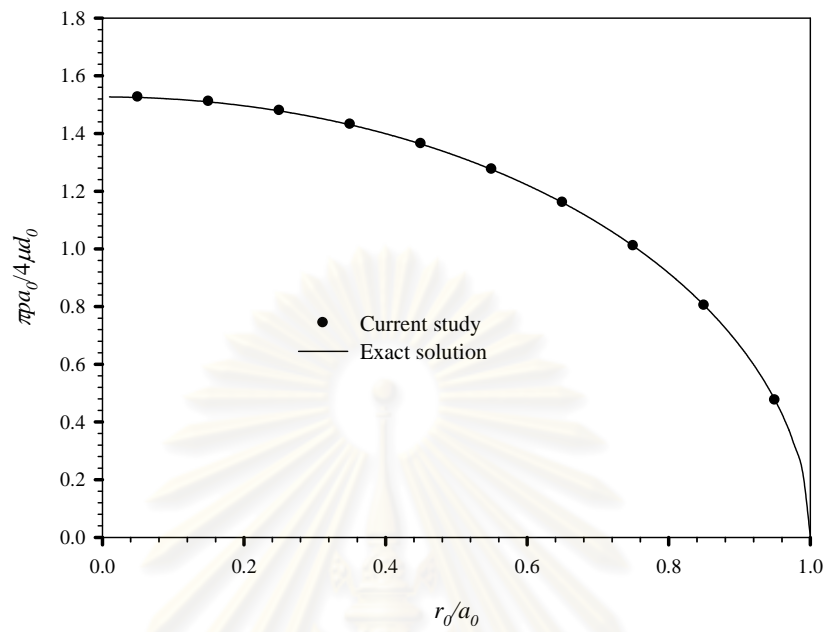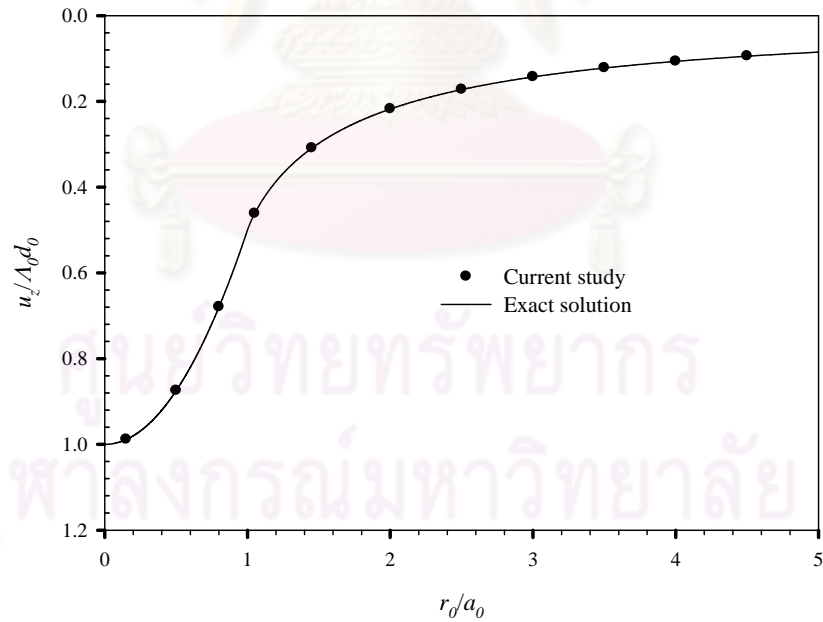
(a)
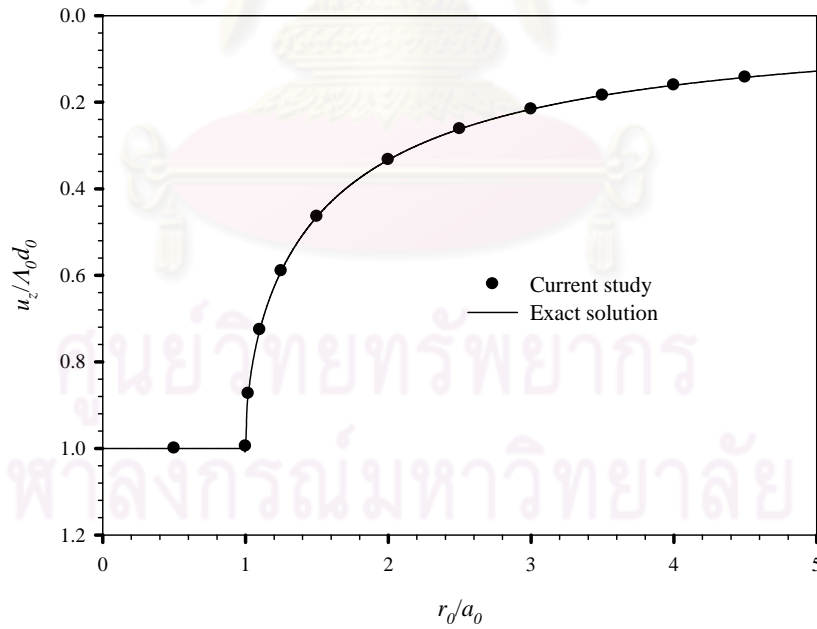
(b)

Figure 4.2 Comparisons of classical numerical solutions with exact solutions for flat-ended cylindrical punch: (a) normalized contact pressure and (b) normalized vertical displacement

(a)

(b)

Figure 4.3 Comparisons of classical numerical solutions with exact solutions for paraboloidal punch: (a) normalized contact pressure and (b) normalized vertical displacement
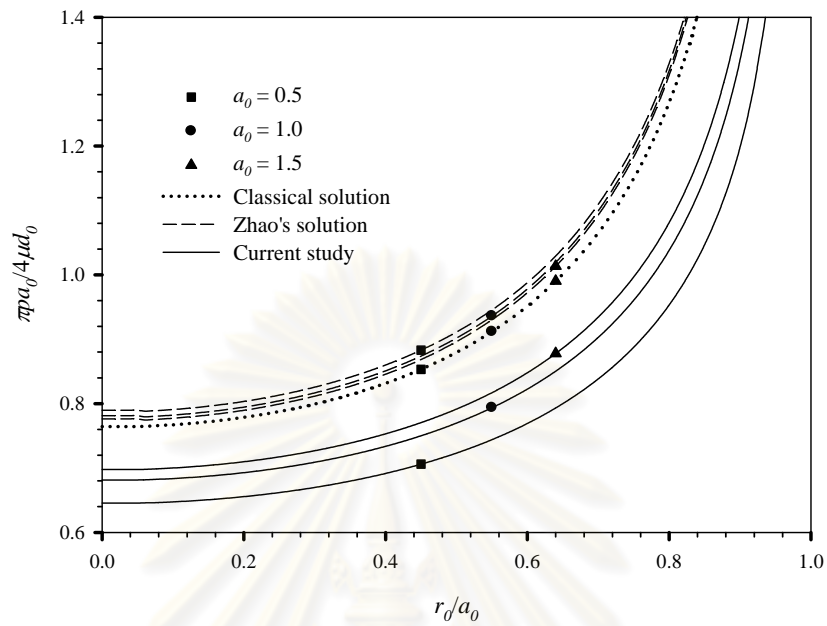
Figure 4.4 Distribution of normalized contact pressure under flat-ended cylindrical punch with various contact radii
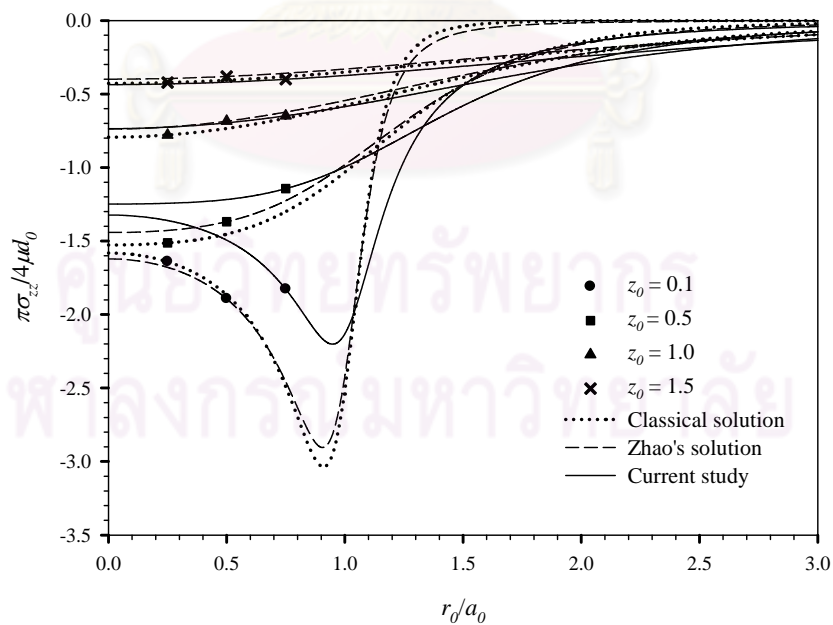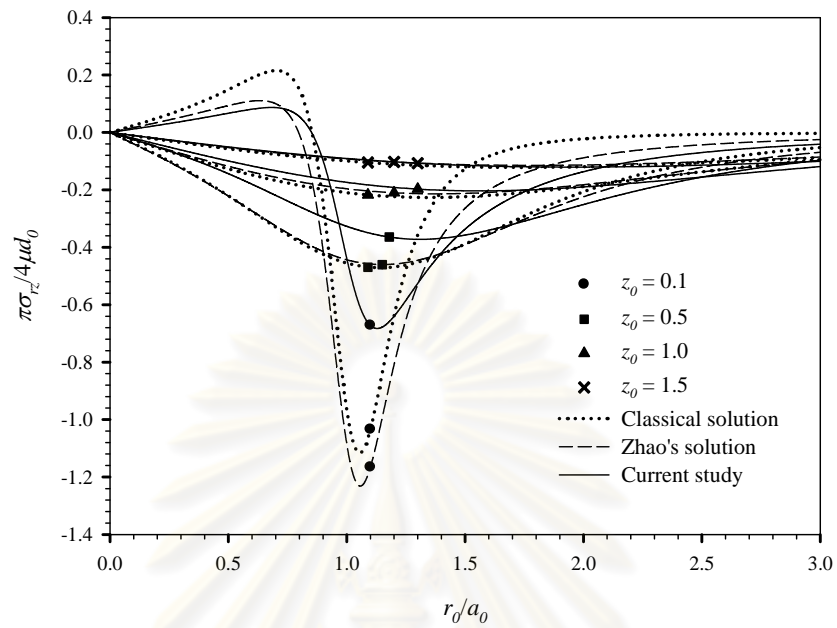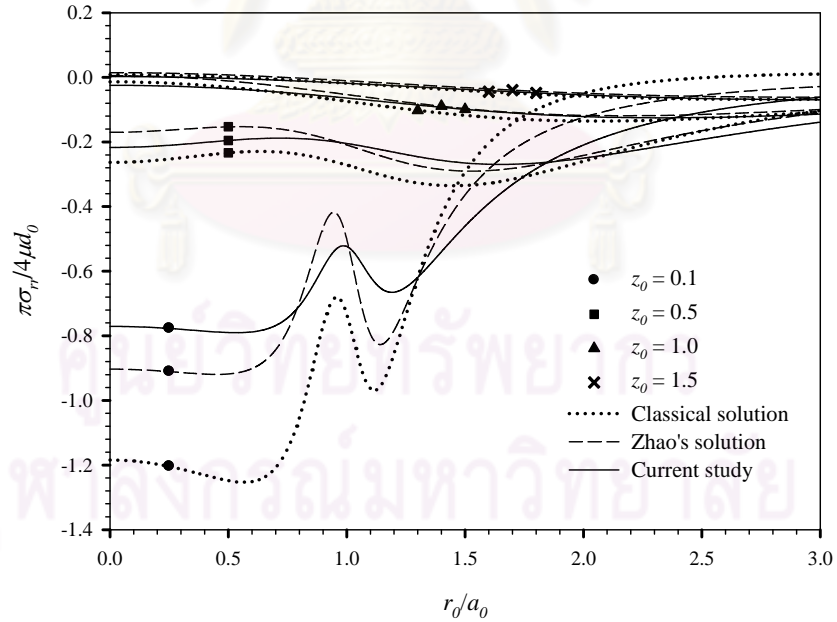

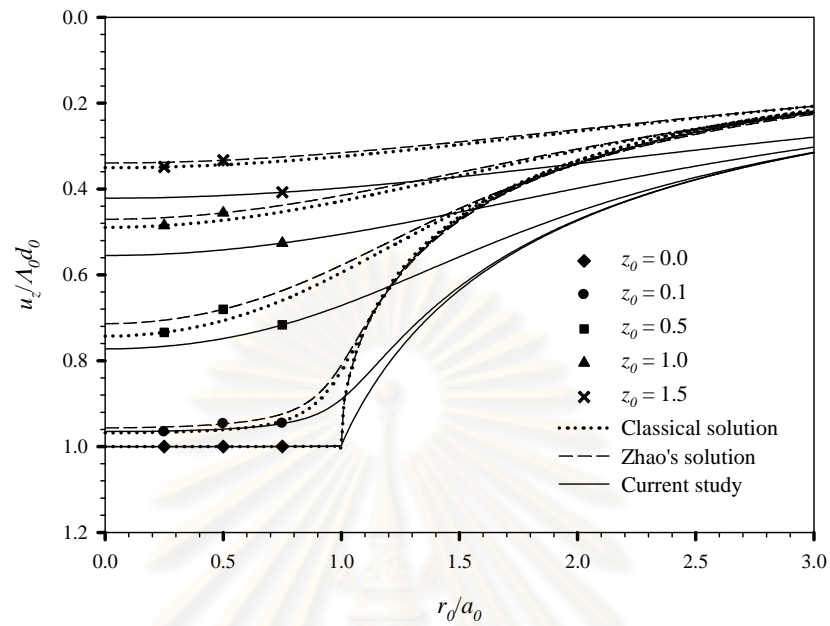Figure 4.5 Normalized vertical stress profiles of flat-ended cylindrical punch with contact radius $a_0 = 0.5$ at various depths
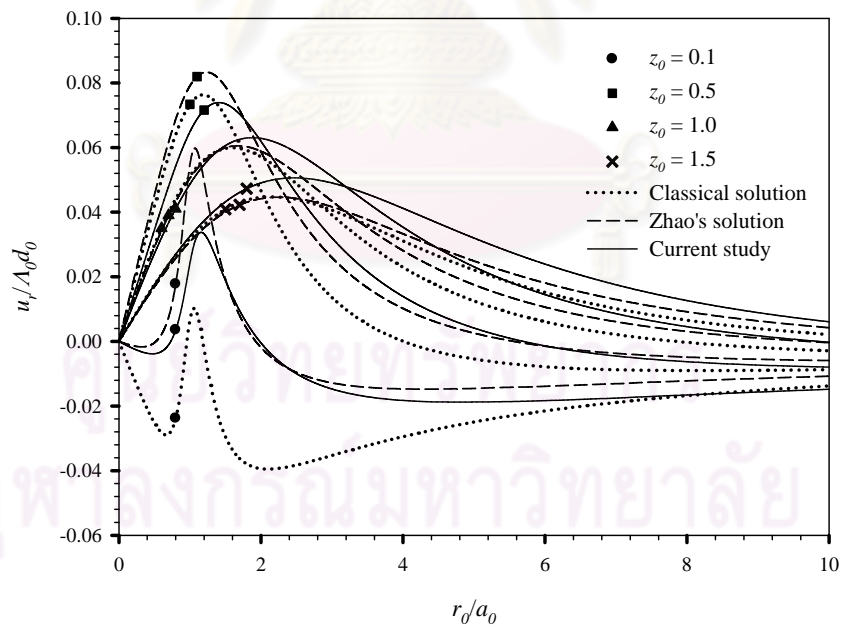
Figure 4.6 Normalized stress profiles of flat-ended cylindrical punch with contact radius $a_0 = 0.5$ at various depths: (a) shear stress and (b) radial stress

Figure 4.7 Normalized displacement profiles of flat-ended cylindrical punch with contact radius $a_0 = 0.5$ at various depths: (a) vertical displacement and (b) radial displacement

4.2.2 Paraboloidal Punch

Consider next a paraboloidal punch with $\alpha_0 = 0.5$ acting on the half-space with the indentation depth d and final contact radius a as shown in Figure 4.1(b). This punch belongs to a class of smooth contact punches since $d\delta/dr$ is well-defined at $r = a$ where a is unknown a priori. Note again that the final contact radius a is determined by enforcing the continuity condition of the vertical stress beneath the punch at $r = a$. Numerical results for elastic fields of this particular punch profile are reported in Figures 4.8-4.11, additionally, some interesting results demonstrating size-dependent behavior and material stiffness due to surface energy effects are finally shown in Figures 4.12-4.14 and all crucial remarks are summarized as follows.

To demonstrate the size-dependency resulting from the influence of surface energy effects, the distribution of normalized contact pressure under a paraboloidal punch, $\pi p a_0/4\mu d_0$, is first presented in Figure 4.8 for three values of the contact radii, $a_0 = 0.5$, 0.8 and 1.0. Interestingly, the contact pressure predicted by the current model becomes finite at the boundary while that obtained from the classical case and Zhao's model vanishes at the boundary of the contact region. Unlike results for the flat-ended cylindrical punch, the contact pressure obtained from the current model is significantly larger than those obtained from the other two models. However, such discrepancy becomes smaller when the contact radius is larger. Note in addition that, upon the proper normalization, the distribution of the contact pressure for the classical case is obviously independent of the contact radius and exhibit no size-dependency.

Normalized vertical stress profiles for the paraboloidal punch with a fixed contact radius $a_0 = 0.5$ at five depths, $z_0 = 0.0$, 0.1, 0.5, 1.0 and 1.5, are reported in Figure 4.9. It is important to emphasize that due to the enforcement of continuity of the vertical stress at $r = a$, the singularity behavior at the boundary of the contact region as that observed in the case of flat-ended punch disappears for this particular punch profile. The maximum value of the vertical stress occurs at the origin and rapidly decays to zero as r_0 increases. Clearly, the distribution of the vertical stress along the radial direction at a very small depth exhibits significant difference from the case of the flat-ended punch. Again, the vertical stress very near the free surface

predicted by the current model deviates from those obtained from the classical and Zhao's models and this implies the significant influence of the surface energy effects and the out-of-plane contribution of the residual surface tension.

Figure 4.10(a) and Figure 4.10(b) show the normalized shear and radial stresses along the radial direction with contact radius $a_0 = 0.5$ at four different depths, $z_0 = 0.1$, 0.5, 1.0 and 1.5. Similar to the case of flat-ended punch, the shear stress at each depth increases from zero at $r_0 = 0$ to its peak value near the punch boundary ($r_0/a_0 = 1$) and then decays rapidly as r_0 increases whereas the radial stress decreases monotonically from its maximum value at $r_0 = 0$ as r_0 increases. Again, the surface energy exhibits significant influence on both shear and radial stresses only in a local region very near the punch and its contribution becomes negligible at regions very far from the punch. The influence of surface energy on the vertical and radial displacements is also clearly demonstrated by results shown in Figure 4.11(a) and Figure 4.11(b). The vertical displacement predicted by the current model is comparatively higher with a slower decay rate when compared with those obtained from the other two models. This observed behavior is similar to the case of flat-ended punch.

To further demonstrate the size-dependent behavior, the relationship between the ratio a_0/a_c (where a_c denotes the contact radius for the classical case) and the contact radius a_0 of a paraboloidal punch is investigated and results are shown in Figure 4.12. Due to the influence of surface energy effects, it is evident that the contact radius is smaller than that obtained from the classical case for the same indentation depth. This implies that presence of the surface stress renders the material stiffer. In particular, the difference from the classical solution is less than 1% for Zhao's model and up to 30% for the current model. It appears that the out-of-plane contribution of residual surface tension strongly influences on material stiffness and the surface energy effects play a prominent role in mechanical properties of materials.

Another set of results that confirms the size-dependent behavior of predicted solutions when the surface energy effects are incorporated is associated with the relationship between the normalized indentation force, P/P_c, and the contact radius a_0

for flat-ended cylindrical and paraboloidal punches as shown in Figure 4.13. It is obviously seen that, when the radius of the punch becomes smaller, the indentation force required to produce the same indentation depth is relatively higher due to the surface energy effects. The discrepancy is more pronounced for results predicted by the current model when compared with Zhao's solutions. This implies that the stiffness of materials characterized by the indentation experiment does not only depend on the penetration depth but also highly depend on the radius of the punch. In particular, at the contact radius $a_0 = 0.1$, results obtained from Zhao's model are approximately 5% higher than the classical solution for both punch profiles whereas those predicted by a model accounted for the out-of-plane contribution of the residual surface tension are up to 120% and 160% higher than that obtained from the classical model for paraboloidal and flat-ended punches, respectively.

To clearly demonstrate the influence of surface energy effects on the material stiffness, the relationship between normalized indentation force, $P/4\mu\Lambda_0^2$, and the indentation depth d_0 for both punch profiles are presented in Figure 4.14(a) and Figure 4.14(b). It can be concluded from these results that the indentation force for both punches predicted by the current model is significantly higher than that obtained from the classical model and Zhao's model. This additionally confirms that materials become stiffer due to the presence of the surface stress effects and the out-of-plane contribution of the residual surface tension amplifies such influence. It is also important to emphasize that the discrepancy of results for the flat-ended cylindrical punch is more pronounced than that for the paraboloidal punch due to the non-smoothness of the punch profile and the singularity of stress field introduced at the boundary of the contact region.
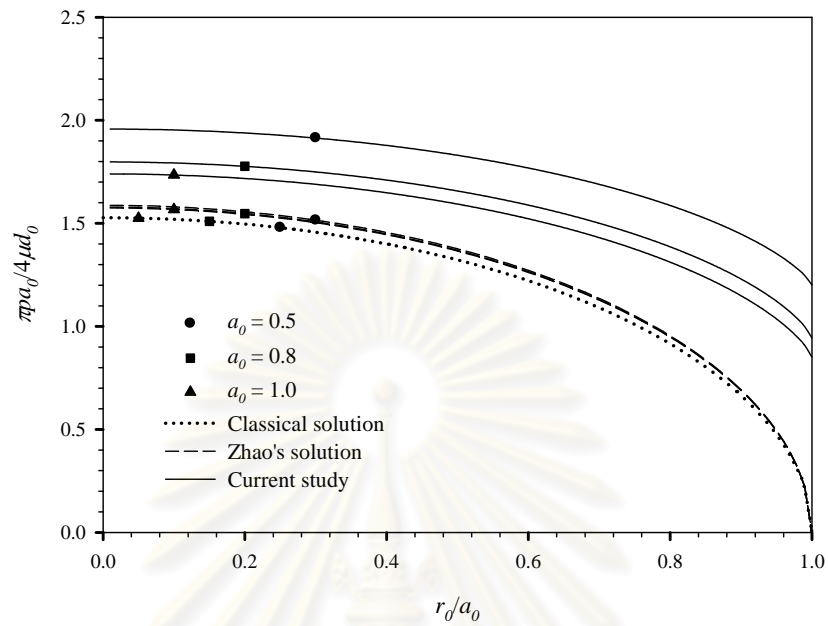
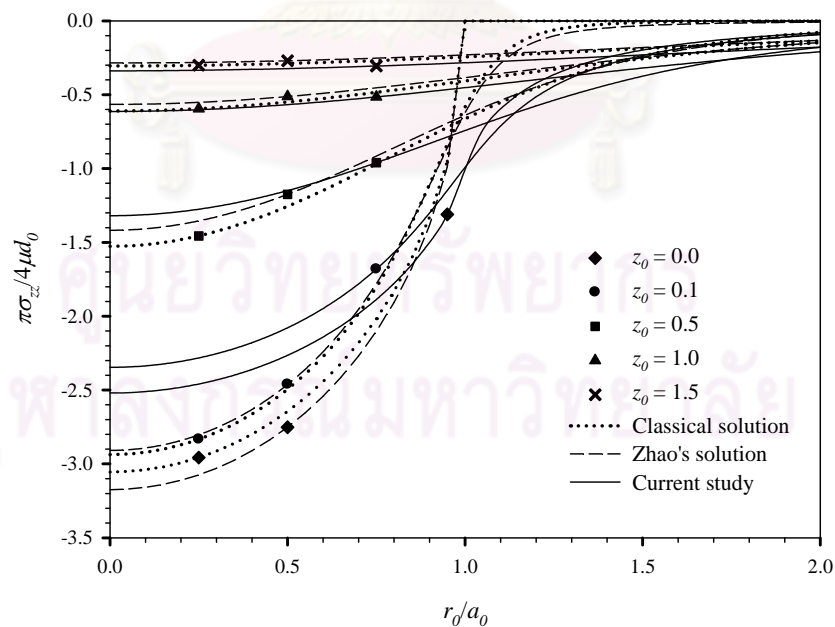Figure 4.8 Distribution of normalized contact pressure under paraboloidal punch with various contact radii
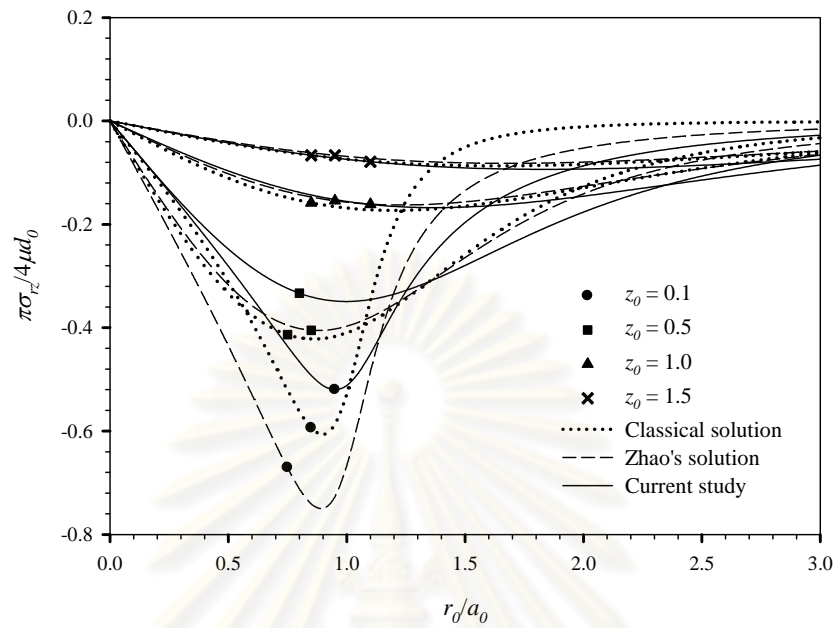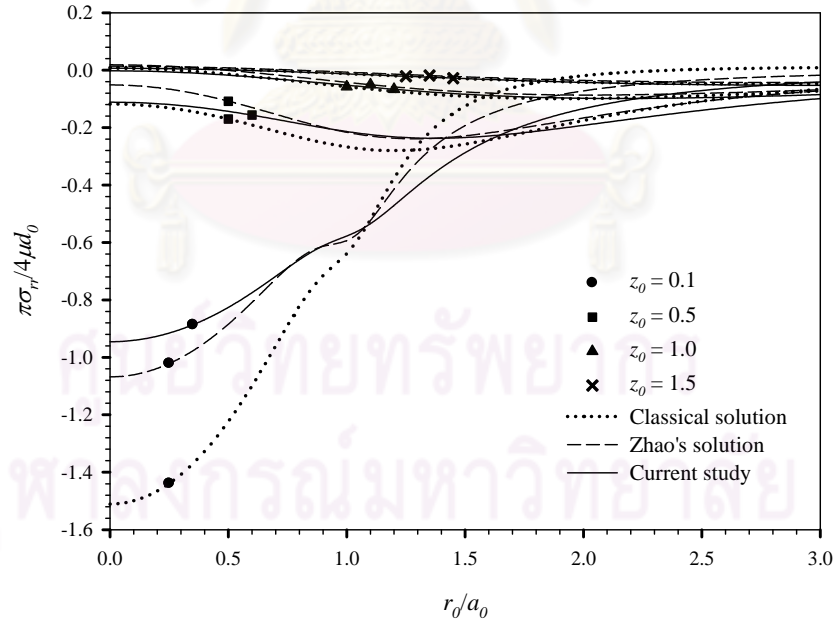

Figure 4.9 Normalized vertical stress profiles of paraboloidal punch with contact radius $a_0 = 0.5$ at various depths

Figure 4.10 Normalized stress profiles of paraboloidal punch with contact radius $a_0 =$ 0.5 at various depths: (a) shear stress and (b) radial stress
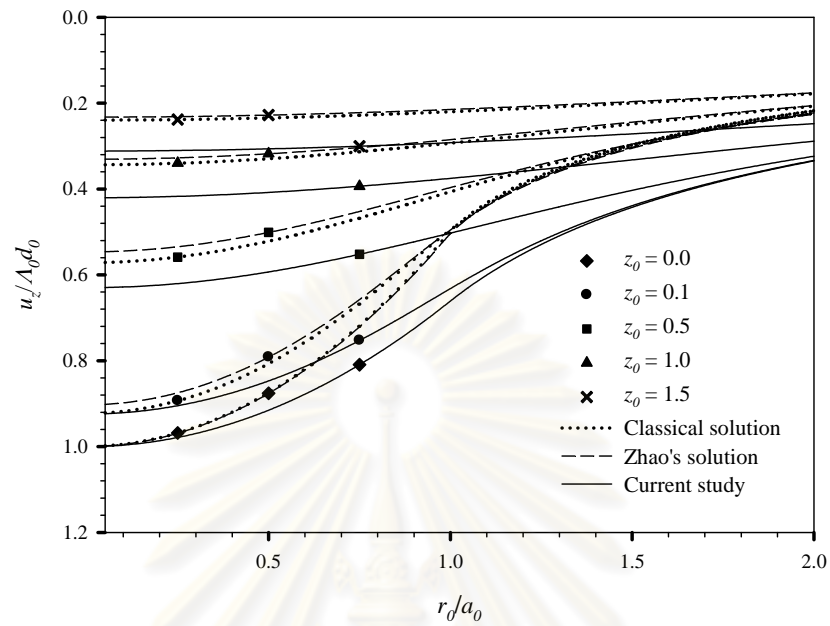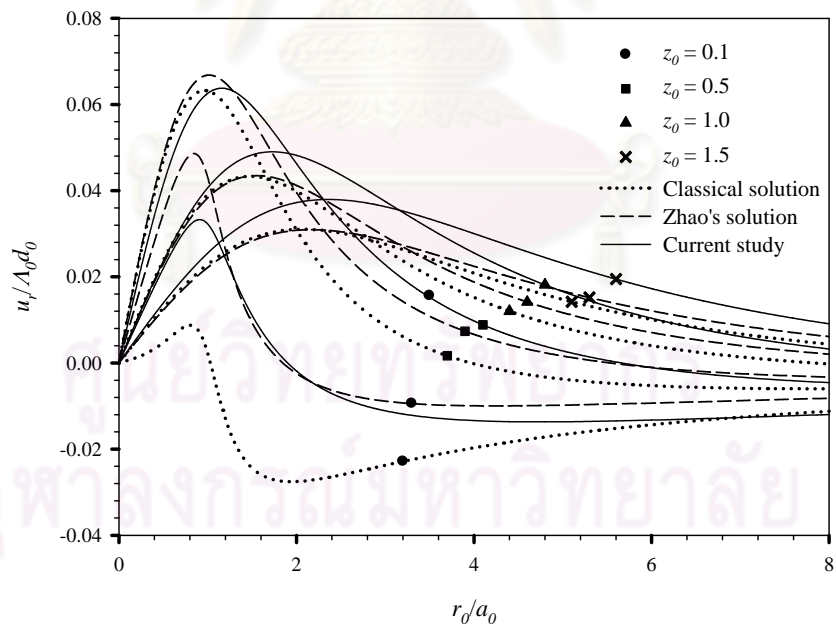
Figure 4.11 Normalized displacement profiles of paraboloidal punch with contact radius $a_0 = 0.5$ at various depths: (a) vertical displacement and (b) radial displacement
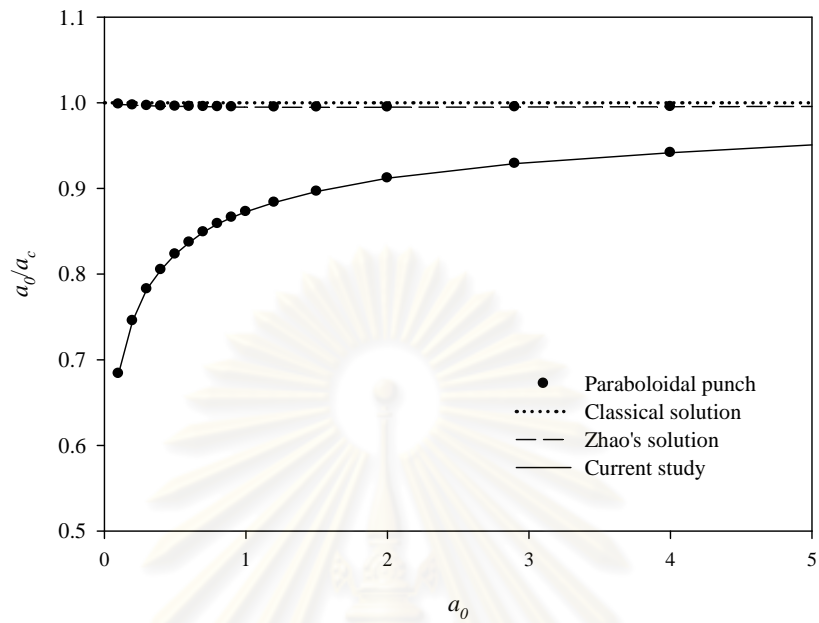
Figure 4.12 Variation of a_0/a_c versus contact radius a_0.
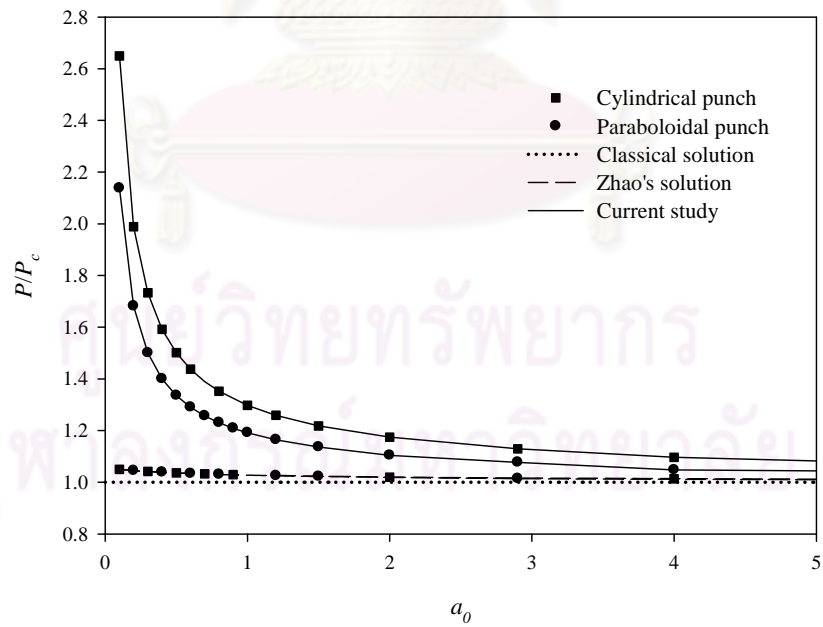
Figure 4.13 Variation of normalized indentation force versus contact radius a_0
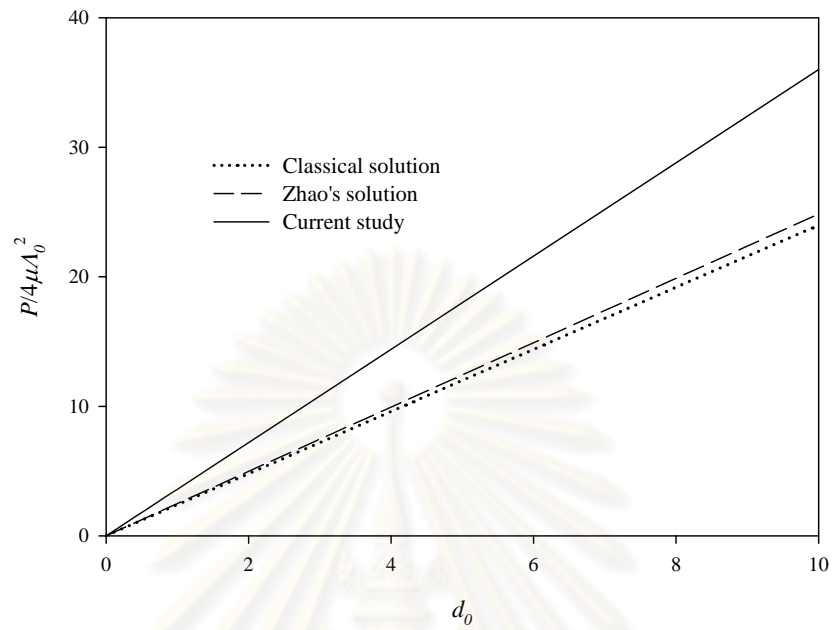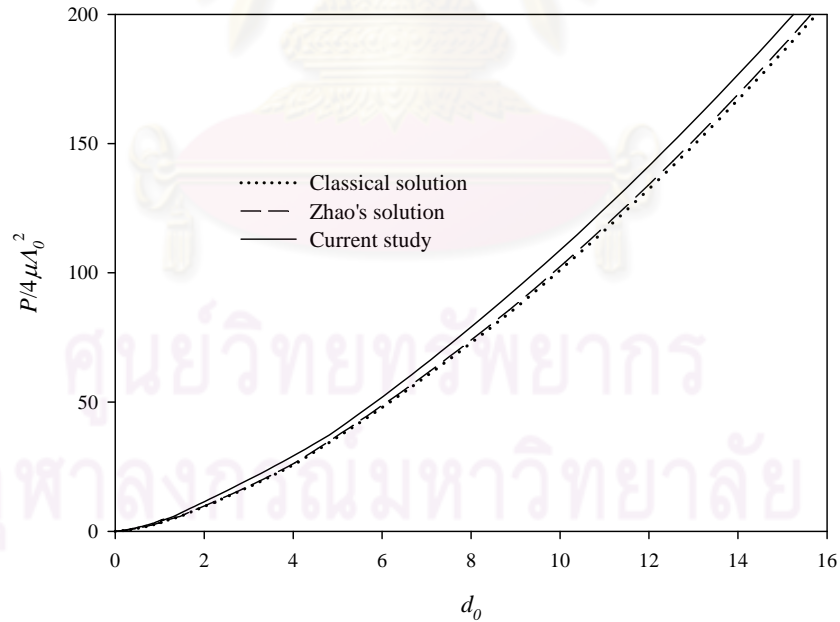
Figure 4.14 Relationship between normalized indentation force and indentation depth
d_0: (a) flat-ended cylindrical punch and (b) paraboloidal punch

Table 4.1 Material properties used in numerical study

Model Parameter	Value (unit)
λ	58.17×10^9 (N/m^2)
μ	26.13×10^9 (N/m^2)
Λ_0	0.16707 (nm)
λ^s	6.8511 (N/m)
μ^s	-0.376 (N/m)
τ^s	1 (N/m)

ศูนย์วิทยทรัพยากร
จุฬาลงกรณ์มหาวิทยาลัย

CHAPTER V

CONCLUSIONS

5.1 Summary and Major Findings

The complete solutions of an axisymmetric rigid frictionless indentation acting on an isotropic, elastic half-space with consideration of surface energy effects by employing a complete version of Gurtin-Murdoch surface elasticity model have been fully investigated. Based on the axisymmetric solutions in term's of Love's strain potential together with the application of Hankel integral transform technique, the mixed boundary conditions on the surface of a half-space both outside and inside the contact region can be reduced to a set of dual integral equations which can be further equivalently transformed into a single Fredholm integral equation of the second kind. To obtain the solution of this single integral equation, various numerical schemes have been employed to enhance both the accuracy and computational efficiency of the solutions. First, standard approximation of a solution form and a collocation technique are adopted to discretize the Fredholm integral equation. After a system of linear algebraic equations with nonsymmetric, dense coeffient matrix is obtained from the discretization, either LU-decomposition or stabilized bi-conjugate gradient method has been applied to solve such a system. Finally, complete elastic fields within the half-space are obtained by applying the Hankel innversion along with using standard Gaussian quadrature. For smooth-contact punches, a physically admissible condition associated with the continuity of vertical stress at the contact boundary is employed to determine the unknown contact radius for a given indentation depth.

The numerical procedures have been implemented as an in-house computer code to determine the complete elastic fields of both non-smooth contact and smooth contact punches. The validity of the current formulation and accuracy of the numerical implementations have been confirmed by comparing with the classical case in which exact solutions exist. As anticipated, obtained numerical results have demonstrated that the influence of surface energy effects becomes larger when the

size of the punch is smaller especially in the region very near the punch. In addition, material behaves stiffer due to such effects. It is interestingly remarked that the distribution of contact pressure for two punch profiles (i.e. flat-ended and paraboloidal punches) obtained from the current model exhibits significant discrepancy. In particular, the contact pressure obtained from the current model for the flat-ended punch is considerable lower than the classical case and that by Zhao (2009) whereas, for the paraboloidal punch, the current model predicts much higher contact pressure than the other two models. However, for both types of contacts, elastic fields obtained from the current model indicate the strong influence of the surface free energy for region relatively close to the punch. Such influence decays rapidly for the vertical stresses but, for the vertical displacements, it exhibits slower decay as the depth increases. Still, the sigularity at the boundary has been observed for the case of a non-smooth contact. Size-dependent behavior has been also presented to confirm the essence of accounting surface energy effects on analysis of material properties at nanoscale and soft elastic solids due to their high surface to volume ratio.

5.2 Suggestions for Future Work

The boundary value problem focused on in the current study is restricted only to the axisymmetric indentation on an isotropic, elastic half-space. In addition, the punch is also assumed to be rigid with no friction. The generalization to alleviate all those limitations should be potentially useful to enhance understanding of nanomechanics and the mechanics of soft solids in a broader context. For instance,

(i)   A punch profile can be generalized to non-axisymmetric one and an elastic half-space can also be replaced by a more general film/substrate system.

(ii)   A constitutive model for an elastic half-space can be generalized to treat both anisotropic linearly elastic and inelastic materials. The ability to treat material anisotropy and nonlinear material behavior will enhance the modeling capability for simulating more practical

problems associated with characterization of material properties using nanoindentations.

(iii) A proper friction model can be incorporated to treat the interaction between a punch and an elastic half-space. It is known that frictionless contact is very idealistic and can hardly be found in practices.

REFERENCES

Armstrong, R. W., Shin, H., and Ruff, A. W. 1995. Elastic/plastic effects during very low-load hardness testing of copper. Acta Metallurgica et Materialia 43: 1037-1043.

Beegan, D., Chowdhury, S., and Laugier, M. T. 2007. Comparison between nanoindentation and scratch test hardness (scratch hardness) values of copper thin films on oxidised silicon substrates. Surface and Coatings Technology 201: 5804-5808.

Booker, R., and Boysen, E. 2005. Nanotechnology for dummies. New Jercy: Wiley.

Boussinesq, J. 1885. Applications des Potentiels à l' Étude de l' Équilibre et du Mouvement des Solides Élastiques. Paris: Gauthier-Villars.

Cammarata, R. C. 1994. Surface and interface stress effects in thin films. Progress in Surface Science 46: 1-38.

Cammarata, R. C. 1997. Surface and interface stress effects on interfacial and nanostructured materials. Materials Science and Engineering A 237: 180-184.

Chaudhuri, P. K., and Ray, S. 2003. Effects of an axisymmetric rigid punch on a nonhomogeneous transversely isotropic half-space. Australian & New Zealand Industrial and Applied Mathematics Journal 44: 461–474.

Chen, C. S., Wang, C. K., and Chang, S. W. 2008. Atomistic simulation and investigation of nanoindentation, contact pressure and nanohardness. Interaction and Multiscale Mechanics 1: 411-422.

Chen, W. 2000. On piezoelastic contact problem for a smooth punch. International Journal of Solids and Structures 37: 2331-2340.

Clements, D. L. 1971. The indentation of an anisotropic half space by a rigid punch. Journal of the Australian Mathematical Society 12: 75-82.

Dhaliwal, R. S., and Rau, I. S. 1970. The axisymmetric boussinesq problem for a thick elastic layer under a punch of arbitrary profile. International Journal of Engineering Science 8: 843-856.

Dingreville, R., and Qu, J. 2007. A semi-analytical method to compute surface elastic properties. Acta Materialia 55: 141-147.

Dingreville, R., Qu, J., and Cherkaoui, M. 2005. Surface free energy and its effect on the elastic behavior of nano-sized particles, wires and films. Journal of the Mechanics and Physics of Solids 53: 1827-1854.

Doerner, M. F., and Nix, W. D. 1986. A method for interpreting the data from depth-sensing indentation instruments. Journal of Materials Research 1: 601-609.

Duan, H. L., Wang, J., Huang, Z. P., and Karihaloo, B. L. 2005. Eshelby formalism for nano-inhomogeneities. Proceedings of the Royal Society A 461: 3335-3353.

Eshelby, J. D., Read, W. T., and Shockley, W. 1953. Anisotropic elasticity with applications to dislocation theory. Acta Metallurgica 1: 251-259.

Fischer, F. D., Waitz, T., Vollath, D., and Simha, N. K. 2008. On the role of surface energy and surface stress in phase-transforming nanoparticles. Progress in Materials Science 53: 481-527.

Gao, Y. F., Xu, H. T., Oliver, W. C., and Pharr, G. M. 2008. Effective elastic modulus of film-on-substrate systems under normal and tangential contact. Journal of the Mechanics and Physics of Solids 56: 402-416.

Giannakopoulos, A. E., and Parmaklis, A. Z. 2007. The contact problem of a circular rigid punch on piezomagnetic materials. International Journal of Solids and Structures 44: 4593–4612.

Gibbs, J. W. 1906. The scientific papers of J. Willard Gibbs. Vol. 1. London: Longmans Green.

Gurtin, M. E., and Murdoch, A. I. 1975. A continuum theory of elastic material surfaces. Archive for Rational Mechanics and Analysis 57: 291-323.

Gurtin, M. E., and Murdoch, A. I. 1978. Surface stress in solids. International Journal of Solids and Structures 14: 431-440.

Gurtin, M. E., Weissmüller, J., and Larché, F. 1998. A general theory of curved deformable interfaces in solids at equilibrium. Philosophical Magazine A 78: 1093-1109.

Hainsworth, S. V., and Page, T. F. 1994. Nanoindentation studies of the chemomechanical effect in sapphire. Journal of Materials Science 29: 5529-5540.

Harding, J. W., and Sneddon, I. N. 1945. The elastic stresses produced by the indentation of the plane surface of a semi-infinite elastic solid by a rigid punch. Mathematical Proceedings of the Cambridge Philosophical Society 41: 16-26.

He, L. H., and Lim, C. W. 2006. Surface green function for a soft elastic half-space: Influence of surface stress. International Journal of Solids and Structures 43: 132–143.

He, L. H., Lim, C. W., and Wu, B. S. 2004. A continuum model for size-dependent deformation of elastic films of nano-scale thickness. International Journal of Solids and Structures 41: 847–857.

Huang, D. W. 2008. Size-dependent response of ultra-thin films with surface effects. International Journal of Solids and Structures 45: 568-579.

Hughes, T. J. R. 2000. The finite element method: Linear static and dynamic finite element analysis. New Jersey: Dover Publications.

Iijima, S. 1991. Helical microtubules of graphitic carbon. <u>Nature</u> 354: 56-58.

Iijima, S., and Ichihashi, T. 1993. Single-shell carbon nanotubes of 1-nm diameter. <u>Nature</u> 363: 603-605.

Intarit, P., Senjuntichai, T., and Rajapakse, R. K. N. D. 2010. Dislocations and internal loading in a semi-infinite elastic medium with surface stresses. <u>Engineering Fracture Mechanics</u> 77:3592-3603.

Jing, G. Y., et al. 2006. Surface effects on elastic properties of silver nanowires: Contact atomic-force microscopy. <u>Physical Review B</u> 73: 235409.

Lebedev, N. N., and Ufliand, I. S. 1958. Axisymmetric contact problem for an elastic layer. <u>Journal of Applied Mathematics and Mechanics</u> 22: 442-450.

Liao, F., Girshick, S. L., Mook, W. M., Gerberich, W. W., and Zachariah, M. R. 2005. Superhard nanocrystalline silicon carbide films. <u>Applied Physics Letters</u> 86: 171913.

Liu, C. L., Fang, T. H., and Lin, J. F. 2007. Atomistic simulations of hard and soft films under nanoindentation. <u>Materials Science and Engineering A</u> 452-453: 135-141.

Lu, C., Gao, Y., Michal, G., Huynh, N. N., Zhu, H. T., and Tieu, A. K. 2009. Atomistic simulation of nanoindentation of iron with different indenter shapes. <u>Proceedings of the Institution of Mechanical Engineers</u> 223: 997984.

Lu, P., He, L. H., Lee, H. P., and Lu, C. 2006. Thin plate theory including surface effects. <u>International Journal of Solids and Structures</u> 43: 4631-4647.

Lucas, B. N., Hay, J. C., and Oliver, W. C. 2003. Using multidimensional contact mechanics experiments to measure poisson's ratio. <u>Journal of Materials Research</u> 19: 58-65.

Mandal, B. N. 1988. A note on Bessel function dual integral equation with weight function. International Journal of Mathematics and Mathematical Sciences 11: 543-550.

Mao, S. X., Zhao, M., and Wang, Z. L. 2003. Nanoscale mechanical behavior of individual semiconducting nanobelts. Applied Physics Letters 83: 993-995.

Miller, R. E., and Shenoy, V. B. 2000. Size-dependent elastic properties of nanosized structural elements. Nanotechnology 11: 139-147.

Oliver, W. C., and Pharr, G. M. 1992. An improved technique for determining hardness and elastic modulus using load and displacement sensing indentation experiments. Journal of Materials Research 7: 1564-1583.

Peng, B., et al. 2008. Measurements of near-ultimate strength for multiwalled carbon nanotubes and irradiation-induced crosslinking improvements. Nature Nanotechnology 3: 626-631.

Poncharal, P., Wang, Z. L., Ugarte, D., and de Heer, W. A. 1999. Electrostatic deflections and electromechanical resonances of carbon nanotubes. Science 283: 1513-1516.

Povstenko, Y. Z. 1993. Theoretical investigation of phenomena caused by heterogeneous surface tension in solids. Journal of the Mechanics and Physics of Solids 41: 1499-1514.

Ratner, M., and Ratner, D. 2002. Nanotechnology: A gentle introduction to the next big idea. New Jercy: Prentice Hall.

Rau, I. S., and Dhaliwal, R. S. 1972. Further considerations on the axisymmetric boussinesq problem. International Journal of Engineering Science 10: 659-663.

Sander, D. 2003. Surface stress: Implications and measurements. Current Opinion in Solid State and Materials Science 7: 51-57.

Selvadurai, A. P. S. 2000. <u>Partial differential equations in mechanics 2</u>. Germany: Springer.

Sharma, P., and Wheeler, L. T. 2007. Size-dependent elastic state of ellipsoidal nano-inclusions incorporating surface∕interface tension. <u>Journal of Applied Mechanics - Transactions of the ASME</u> 74: 447-454.

Sharma, P., Ganti, S., and Bhate, N. 2003. Effect of surfaces on the size-dependent elastic state of nano-inhomogeneities. <u>Applied Physics Letters</u> 82: 535-537.

Shenoy, V. B. 2002. Size-dependent rigidities of nanosized torsional elements. <u>International Journal of Solids and Structures</u> 39: 4039–4052.

Shenoy, V. B. 2005. Atomistic calculations of elastic properties of metallic fcc crystal surfaces. <u>Physical Review B</u> 71: 094104.

Shuttleworth, R. 1950. The surface tension of solids. <u>Proceedings of the Physical Society Section A</u> 63: 444-457.

Sinnott, S. B., Colton, R. J., White, C. T., Shenderova, O. A., Brenner, D. W., and Harrison, J. A. 1997. Atomistic simulations of the nanometer-scale indentation of amorphous-carbon thin films. <u>Journal of Vacuum Science and Technology A</u> 15: 936-940.

Sneddon, I. N. 1951. <u>Fourier transform</u>. New York: McGraw-Hill.

Sneddon, I. N. 1965. The relation between load and penetration in the axisymmetric boussinesq problem for a punch of arbitrary profile. <u>International Journal of Engineering Science</u> 3: 47-57.

Sneddon, I. N. 1966. <u>Mixed boundary value problems in potential theory</u>. New York: John Wiley & Sons.

Stroh, A. N. 1958. Dislocations and cracks in anisotropic elasticity. <u>Philosophical Magazine</u> 3: 625-646.

Tian, L., and Rajapakse, R. K. N. D. 2007a. Analytical solution for size-dependent elastic field of a nanoscale circular inhomogeneity. <u>Journal of Applied Mechanics - Transactions of the ASME</u> 74: 568-574.

Tian, L., and Rajapakse, R. K. N. D. 2007b. Elastic field of an isotropic matrix with a nanoscale elliptical inhomogeneity. <u>International Journal of Solids and Structures</u> 44: 7988-8005.

Wang, W., Zeng, X., and Ding, J. 2010. Finite element modeling of two-dimensional nanoscale structures with surface effects. <u>World Academy of Science, Engineering and Technology</u> 72: 867-872.

Wong, E. W., Sheehan, P. E., and Lieber, C. M. 1997. Nanobeam mechanics: Elasticity, strength, and toughness of nanorods and nanotubes. <u>Science</u> 277: 1971-1975.

Yakobson, B. I. 2003. Nanomechanics. In W. A. Goddard; D. W. Brenner; S. E. Lyshevski; and G. J. Iafrate (eds.), <u>Handbook of nanoscience, engineering, and technology</u>, chapter 17. Florida: CRC Press.

Yang, F. 1998. Indentation of an incompressible elastic film. <u>Mechanics of Materials</u> 30: 275-286.

Yang, F., and Li, J. C. M. 1995. Impression test of 63Sn-37Pb eutectic alloy. <u>Materials Science and Engineering A</u> 201: 40-49.

Yang, F., and Li, J. C. M. 1997. Viscosity of selenium measured by impression test. <u>Journal of Non-Crystalline Solids</u> 212: 136-142.

Yang, Y. T., et al. 2001. Monocrystalline silicon carbide nanoelectromechanical systems. <u>Applied Physics Letters</u> 78: 162-164.

Yu, H. Y., Sanday, S. C., and Rath, B. B. 1990. The effect of substrate on the elastic properties of films determined by the indentation test-axisymmetric boussinesq problem. <u>Journal of the Mechanics and Physics of Solids</u> 38: 745-764.

Zhao, X. J. 2009. <u>Surface loading and rigid indentation of an elastic layer with surface energy effects</u>. Master's thesis, Faculty of graduate studies (mechanical engineering). The university of british columbia (vancouver).

Zhao, X. J., and Rajapakse, R.K.N.D. 2009. Analytical solutions for a surface-loaded isotropic elastic layer with surface energy effects. <u>International Journal of Engineering Science</u> 47: 1433-1444.

BIOGRAPHY

The author, Miss. Yutiwadee Pinyochotiwong graduated her Bachelor of Engineering degree in Civil Engineering from Chulalongkorn University in 2008. As she would like to obtain the advanced knowledge of structural engineering, she continued her Master's degree in structural civil engineering at Chulalongkorn University in the same year under the supervision of Assistant Professor Dr. Jaroon Rungamornrat and Professor Dr. Teerapong Senjuntichai. For two years of studying in Master's degree, she had studied new interesting knowledge of advanced solid mechanics solved by the powerful numerical techniques and decided to do her research on this kind of field. She successfully fulfilled the requirements for the Master of Engineering degree in 2010.